5-31-2020

Enhanced removal of perfluorooctanoic acid (PFOA) via microwave-fenton-reactive membrane filtration

Fangzhou Liu
New Jersey Institute of Technology

ABSTRACT

ENHANCED REMOVAL OF PERFLUOROOCTANOIC ACID (PFOA) VIA MICROWAVE-FENTON-REACTIVE MEMBRANE FILTRATION

by
Fangzhou Liu

Perfluorooctanoic Acid (PFOA), one of the common per- and poly fluorinated alkylated substances (PFASs), is increasingly detected in the environment due to the diverse industrial applications and high resistance to degradation processes. This study evaluated degradation of PFOA in microwave-assistant catalytic membrane filtration, a process that integrates microwave catalytic reactions into a ceramic membrane filtration. First, water permeation of the pristine and catalyst-coated membranes were examined under the influence of microwave irradiation to analyse the impacts of the coating layer and water temperature increase on permeate flux, which were well interpreted by three models. Then, the PFOA removal was first assessed in a continuous filtration model with and without microwave irradiation. Our results show that PFOA adsorbed on membrane and catalyst materials and fully penetrated the membrane filter after reaching adsorption equilibrium. Under microwave irradiation (7.2 watt·cm^{-2}), approximate 65.9% of PFOA (25 μg·L^{-1}) in the feed solution was degraded within a hydraulic time of 2 min (at the permeate flow rate of 43 LMH) due to the microwave-Fenton like reactions. In addition, low flow rates and moderate catalyst coating densities are critical for optimizing PFOA removal. Finally, potential degradation mechanisms of PFOA were proposed through the analysis of degradation by-products (e.g., PFPeA). The findings may provide new insight into the development of reactive membrane-enabled systems for destruction of refractory PFAS.

ENHANCED REMOVAL OF PERFLUOROOCTANOIC ACID (PFOA) VIA MICROWAVE-FENTON-REACTIVE MEMBRANE FILTRATION

by
Fangzhou Liu

A Thesis
Submitted to the Faculty of
New Jersey Institute of Technology
in Partial Fulfilment of the Requirements for the Degree of
Master of Science in Environmental Engineering

John A. Reif, Jr. Department of Civil and Environmental Engineering

May 2020

Blank Page

APPROVAL PAGE

ENHANCED REMOVAL OF PERFLUOROOCTANOIC ACID (PFOA) VIA MICROWAVE-FENTON-REACTIVE MEMBRANE FILTRATION

Fangzhou Liu

Dr. Wen Zhang, Dissertation Advisor	Date: 4/2/2020
Associate Professor of Civil and Environmental Engineering, NJIT	

Dr. Lucia Rodriguez-Freire, Committee Member	Date: 4/2/2020
Assistant Professor of Civil and Environmental Engineering, NJIT	

Dr. Xianqing Wang, Committee Member	Date:4/2/2020
Associate Professor of Chemical Engineering, NJIT	

BIOGRAPHICAL SKETCH

Author: Fangzhou Liu

Degree: Master of Science

Date: May 2020

Undergraduate and Graduate Education:

- Master of Science in Environmental Engineering,
  New Jersey Institute of Technology, Newark, NJ, 2019

- Bachelor of Science in Environmental Engineering,
  Henan University of Science and Technology University, China, 2014

Major: Environmental Engineering

Presentations and Publications:

1. Fangzhou Liu, Likun Hua, Wen Zhang, Influences of Microwave Irradiation on. Performances of Membrane Filtration and Catalytic Degradation of Perfluorooctanoic Acid (PFOA), Environment International, reviewing
2. Fangzhou Liu, Extraction, Purification and Detection of PFAS in Surface Raw Water. using Agilent LC-QQQ, 2019 EAS. 11/2019
3. Fangzhou Liu, Microwave enhanced membrane filtration system for PFOA degradation, 2019 MAST 10/2019
4. Fangzhou Liu, Microwave-enhanced Membrane Filtration for PFOA degradation.2019. GSA 11/25/2019
5. Fangzhou Liu, Microwave-enhanced Membrane Filtration for degradation of PFASs, 2020 ACS accepted

6. Fangzhou Liu, Influences of Microwave Irradiation on Performances of Membrane Filtration and Catalytic Degradation of Perfluorooctanoic Acid (PFOA). 2020 NAMS. 5/2020 under preparision

ACKNOWLEDGEMENTS

Special thanks go to my dissertation committee members, Dr.Lucia Rodriguez-Freire and Dr. Xianqin Wang. I want to especially thank them for finding time in their busy schedules to review this dissertation and provide considerate advice, important feedback, constructive, and critical comments.

What's more, I want to thank my advisor, Dr.Hsin-Neng Hsieh, who give me responsible, comprehensive, systematic recommendations about my master's degree course, so that I am able to learn more practical knowledge closing to my study. Thanks also go to Dr. Taha F. Marhaba for support of application in CSC scholarship. Additional, Dr. Larisa G Krishtopa, gave me the opportunity of the training of LC-QQQ, helping me to familiar the operation of this instrument as soon as possible. She also helped me troubleshoot the instrument again and again, which largely ensured the progress of my experiment. What's more, I want to appreciate the patient guidance of Dr. Lucia Rodriguez-Freire on my research and assignments of Water Chemistry, enable me to discover and solve the problems of research and learning. Finally, my academic foundation is inseparable from the patient teaching of university teachers. Thanks go to my undergraduate advisor: Dr. Xuefeng Wei. He gave me the opportunity to enter lab and help me to do some fundamental research. In my senior year, he guided me to do experiments and write thesis independently, which greatly aroused my interest in research.

In addition, I want to acknowledge my group members Wanyi Fu, Xiaonan Shi，Chunzhao Chen， Likun Hua, Weihua Qing, Shan xue, Zhifeng Hu, Xiaoyu Wang and Leqi Lin. Wanyi Fu, the first member I met in this group, told me how to be an active, clam and optimistic researcher by her own actions. And I was shocked by her achievements in the academic field，encouraging me to strive to be as good as her. She also often invites us to have dinner together. Xiaonan shi gave me honest advice for my master career and future career plan. If not her sincere help, I couldn't get A in the course of Physical process. In addition, I would like to thank Xiaonan shi and Qingquan Ma for their patience and responsibility in helping me test AFM, which become a very important data in my experiments. Chunzhao Chen，a visiting scholar, teaches me how to standardize paper format，how to search literature quickly and effectively. I want to appreciate the revising and suggesting of Weihua Qing for my paper. Moreover, Leqi Lin, who is a master coming NJIT half year before me, always gives me lots of valuable advice about master's life, and she also is my role model because of her seriously attitude toward research. In addition, I also receive some helps from Ran yan. He drove me to the water plant to take samples, which saved me a lot of experiments and commute time. Shan xue often invited me to her house for dinner and drove me to school to facilitate my study life. Zhifeng Hu and Xiaoyu Wang, who are visiting scholars, shared lots of significant experience of Ph.D in paper writing.

Lastly but the most importantly, I appreciate my parent's long-lasting support, understanding, encouragement, and patience, which accompany me through all the hardship during the research adventure. In particular, my father 's enthusiasm for work always inspired me, he hardly takes any weekends and works hard every day. But he never

complains, he always believes that there will be gains. His attitude towards running also taught me how to do one thing consistently. Even though it was a cold winter and a hot summer, he still insisted to go out for a run in the morning. He never required me to do anything, but his behavior and attitude become the best teacher of my life. I also want to thank my mother for taking care of me. She always knows more about the weather in my area than I do and always reminds me of weather changes. Although we usually don't have much time for video chat, I always feel the warmth of home. I am proud to be part of such a family. Meanwhile, making them proud of me is my endless motivation toward success.

TABLE OF CONTENTS

LIST OF TABLES

CHAPTER 1

INTRODUCTION

1.1 Background and Problem of PFOA

Poly- and perfluoroalkyl substances (PFASs) have been widely utilized in the industrial and commercial field since the 1950s.[1] The carbon-fluorine bonds structure instead of carbon-hydrogen bonds in the molecular chains provided them with excellent chemical and thermal stability. a hydrophilic head group of PFAS provide hydrophilic and hydrophobic properties, as well as high surface activity. With these unique properties, PFASs have been extensively employed in many fields of industries, including electroplating, fire retardants, semiconductor and aviation industries.[2]

As a result of broad applications in industrial products or processes for many decades, PFASs are increasingly found in the environment worldwide.[3-8] The high-energy carbon–fluorine bond render PFASs extremely resistant to natural weathering processes such as hydrolysis, photolysis, and microbial degradation. For instance, the abstraction of fluorine from a carbon atom is thermodynamically unfavorable because the F–OH bond has a dissociation energy at least 216 $kJ\cdot mol^{-1}$ lower than that of the C–F bond (CF_3F 552 $kJ\cdot mol^{-1}$, $R–CF_2–F$ 352 $kJ\cdot mol^{-1}$, $R,R'–CF–F$ 508 $kJ\cdot mol^{-1}$).[9] Furthermore, the electron density of the ionic head group (e.g., carboxylate and sulfonates) is reduced by perfluorination, hindering electron transfer reactions.[10] Perfluorooctanoic acid ($C_7F_{15}COOH$, PFOA) is one of the notable poly- and perfluoroalkyl substances (PFASs), which are regulated by the US EPA drinking water health advisories (70 ng L^{-1}).[11] PFOA is suspected endocrine disrupting compounds and have been shown to bioaccumulate and

cause acute/chronic toxicity in certain organisms.[12] It is reported that long-term contact with such material may increase the risk of kidney cancer, thyroid disease, high plasma lipids, liver and body weight reduction, alveolar wall thickening, mitochondrial damage, gene induction, increases in larval mortality, and increased susceptibility to disease.[13-19] According to the San Antonio Statement and the Madrid Statement,[20, 21] The EPA's health advisory levels (HALs) indicates that drinking water, with individual or combined concentrations of PFOA and PFOS, (below 70 parts per trillion), is not expected to result in adverse health effects over a lifetime of exposure.[22] However a recent report documented that up to 6 million U.S. residents might be exposed to drinking water that exceeds these HALs.[23, 24]

1.2 Challenges in Water Treatment and Application of AOPs

Recent studies have shown that conventional water or wastewater treatment processes are ineffective at removing perfluorochemicals.[25] The Water Research Foundation (WRF) has released assessment results for removing poly- and perfluoroalkyl substances (PFASs) from 13 water and wastewater treatment plants in the United States. The research report (WRF project #4322) indicated that aeration, chlorine dioxide, dissolved air flotation, coagulation, flocculation, sedimentation, granular filtration, and microfiltration are all ineffective for removing PFASs including PFOA and PFOS. Activated carbon and anion exchange are less effective at removing shorter chain PFASs. Recent studies show that nano-filtration (NF) and reverse osmosis (RO) membranes can remove PFAS with high rejection rates (> 95%) [26-31]. However, membrane separation relying on size exclusion may not remove PFASs when the membrane pore sizes are larger than PFASs or their degradation by-products. Again, PFAS-concentrated streams treated by RO and NF

processes, which is approximately 10% of the treated water volume, still requires costly post-treatment or disposal [32]. Accordingly, there is a pressing need for effective separation and complete chemical degradation and destruction in the development of novel treatment technologies.

Novel membrane filtration processes tend to incorporate additional separation or chemical reaction mechanisms. For example, hollow fiber nanofiltration membranes impregnated with poly(m-phenylene isophthalamide) nanomaterials as adsorbents enhanced the removal of PFASs from water. The surface-adsorbed PFAS on membranes were then rinsed off by the methanol solution [33]. Membrane (TS80) filtration combined with powdered activated carbon and hydrotalcite adsorption removed 99% of PFOS and PFOA from water [34]. Apisara et.al proposed a combination of membrane filtration and photocatalysis for the removal of PFOA by sequential nanofiltration and photocatalytic reaction using zero valence iron as catalyst [27]. This new hybrid membrane system not only removed the PFOA, but also degraded the contaminant. Furthermore, a novel $Fe_3O_4@SiO_2-NH_2\&F_{13}$ composite was functionalized onto a silica membrane to enhance the separation of PFAS from water through electrostatic and fluorine-fluorine interactions [35].

Catalytic degradation technologies have been paid increasing attention in PFOA degradation due to its potentially high effectiveness in the degradation and the mineralization of refractory organic pollution, such as photocatalysis, electrochemical catalysis, photo-electrochemical catalysis, catalytic ozonation, and so on. TiO_2 is a widely used photocatalyst because of its availability, non-toxicity, chemical and biological stability, photo-stability and low cost.[36] Wang et al. found that the PFOA degradation

efficiency reached up to 86.7% after 3 h reaction time by adding oxalic acid to TiO_2-mediated photocatalytic process.[37] However, TiO_2 shows low activity for decomposing PFOA under mild condition, or harsh reaction conditions are necessary. Shao et al. reported that the concentration of PFOA declined to limit of detection under 254 nm UV light irradiation within 3 h by using nanostructure β-Ga_2O_3 photocatalyst.[38] Although it was reported that photocatalytic indium oxide (In_2O_3) possesses more prominent activity for PFOA decomposition than TiO_2 due to photogenerated holes in In_2O_3, the defluorination rates of PFOA is still slow. [39, 40] Besides, Huang et.al demonstrate that the defluorination ratio of PFOA by combining process of photocatalysis and ozonation was 4.18 and 3.01 times more than that in UV/O_3 and $UV/TiO_2/O_2$ within 4 h reaction time,[41] because the addition of ozone improved the quantum efficiency of photocatalysis.[42] In addition, electrochemical catalysis has received growing attention due to its strong oxidation performance, mild condition, and environmental compatibility. Recently, a few studies have been carried out regarding the electrochemical degradation of PFOA. [43-45] These reports found that PFOA could be degraded over boron-doped diamond (BDD) film electrode and Ti/SnO2–Sb–Bi electrode due to the electron transfer from PFOA to BDD anode, but the high cost and especially the difficulties to find an appropriate substrate for deposition the diamond layer limit the large-scale application of the BDD electrode. Therefore, it is required to find more economical, eco-friendly and efficient technology for the PFOA degradation.

Coupling advanced oxidation processes (AOPs) with physical membrane filtration has been extensively studied to enable the destruction of organic pollutants [46-49]. Typical AOPs include ultraviolet (UV) irradiation, ozonation (O_3), ozonated air fractionation, UV/O_3,

4

UV/H$_2$O$_2$, electrochemical oxidation or reduction, persulfate, and sonochemical pyrolysis [11, 32, 50]. For example, the degradation of PFOA and PFOS has been achieved via electrooxidation on ceramic membranes coated with or made of Ce-PbO$_2$, boron-doped diamond, and Ti$_4$O$_7$ [24, 45, 51]. Membrane filtration has also been coupled with the use of oxidants, such as ozone and hydrogen peroxide to remove PFAS [27, 32, 52-54]. However, extensive use of these hazardous chemical oxidants reduces economic viability and safety for large-scale utilization. Moreover, the aging or damage of polymeric membranes from non-selective attack by chemical oxidant is another concern. Recently, photocatalytic ceramic membranes (PCMs) have also been intensively studied to enhance the chemical destruction of recalcitrant pollutants [55-58]. However, the practical implementation of PCMs are hampered by UV illumination in industrial membrane processes, where light penetration in tabular and spiral membrane surfaces is almost impossible.

1.3 Microwave Catalysis: principles and current applications

Microwave (MW) is a form of electromagnetic radiation which frequencies range from 300 MHz to 300 GHz and wavelengths ranging between 1 m and 1 m. The consumer microwave ovens widely choose a frequency of 2.45 GHz in order to avoid interference with broadcast and communications bands. Microwave induces dielectric heating process by rotating polar molecules and produce thermal energy.[59] Electric dipoles such as water and ethylene glycol has higher dielectric constant and loss factors, which is able to rotate as they align themselves under microwaves irradiation. Then, heat produced by rotating molecules hit other molecules and promote molecular motion. It is reported that the microwave energy may induce non-thermal effect by the rotation of dipoles and migration of ions, which is able to increase the degradation of refractory matters to some extent.[60]

Microwave technology has widely been adopted in industrial processes, including chemical synthesis, chemical reactions, digestion, drying, pharmaceutical ingredient extraction, food processing, pasteurization and sterilization. For instance, in heterogeneous catalyzed reactions,[61-67] the most obvious advantage with microwave irradiation is the ability to selectively heat catalysts, while allowing the medium to remain at a substantially lower temperature. Many industrial processes utilizing heterogeneous catalysts are high-temperature processes wherein both components of the reaction (i.e., catalyst and medium) are heated to the temperature required for the reaction to occur. There are a number of different classes of heterogeneous catalyst materials that have different microwave absorption processes:[68-74] (1) Solid binary oxides such as SiO_2, Al_2O_3, TiO_2, and ZrO_2, and ternary oxides such as spinels and perovskites. Porous silicate and alumina silicate materials such as zeolites and template mesoporous sieves also fall into this category. (2) Metals: Metal surfaces, such as Ni, Cu, and Ag. (3) Support catalysts: an oxide support with an active site deposited on the surface that performs all or part of the catalytic function. Catalyst-coated reactors have been reported for a variety of chemical synthesis or catalytic conversion with microwave. For example, He et al. used microwave energy to provide heat locally to a heterogeneous Pd supported catalyst onto alumina situated inside a microreactor to achieve highly selective interaction with microwaves.[75] Benaskar and coworkers recently introduced a novel Cu/ZnO catalyst coated as a thin film onto a tubular glass reactor for microwave catalysis.[76] Benaskar et al. also developed a micro-fixed-bed reactor (μ-FBR) using a supported Cu nanocatalyst, which resulted in a significant activity enhancement localized precise control of heating.[77] Commercial microwave injectors can irradiate reactor chambers from different angles to allow sufficient exposure of microwave

energy. Superior to other stimuli such as light illumination or ultrasonication, microwave irradiation can penetrate reactor housing and other cover materials with limited energy loss from penetration.[78] This unique feature will potentially increase reaction specificity on functionalized surface and lower energy cost.

1.4 Microwave-enhanced Membrane Filtration

Microwave-assisted catalytic reactions are recently demonstrated for refractory pollutant degradation, including microwave/persufate/H_2O_2 [79], microwave-Fenton [80, 81] or microwave-Fenton-like [82] and microwave-photo/electro/ultrasonic processes [83-85]. For instance, microwave-enhanced Fenton reactions were combined with Mn^{2+} ion to remove Bisphenol A (BPA) in wastewater [80]. An effective microwave catalyst, $NiCo_2O_4$-$Bi_2O_2CO_3$ composite, also was developed for microwave catalytic oxidation degradation of 4-nitrophenol without adding any oxidant [79]. Moreover, a microwave–Fenton process was applied to remove the RO-generated concentrated leachate [81]. Besides, $BiFeO_3$ (BFO) was used as a Fenton-like catalyst in degradation of rhodamine B (RhB) [86, 87] and PFOA [88]. Our previous study revealed that the removal rate of 1,4-dioxane was enhanced through the BFO-coated ceramic membranes under microwave irradiation, primarily due to the generation of •OH [89]. Besides radicals, microwave energy can be selectively absorbed by BFO catalysts and promote the formation of "hotpots" and nanobubbles that also facilitate chemical reactions by increasing local solution temperatures [90, 91] and effectively enable surface cleaning or membrane defouling [89].

In this study, this microwave- catalytic membrane filtration was employed to treat perfluorooctanoic acid (PFOA)-containing water, showed in **Figure 1.1**. This technology is a patented process that utilizes microwave to catalyze surface reactions on ceramic

membranes that promote degradation of pollutants when they pass through membrane interfaces as illustrate in **Figure 1.2**. The Design-Build-Test -Analyze cycle have been showed in **Figure 1.3**. First, the BFO-coated membranes were characterized with respect to the changes of membrane surface morphology such as roughness. Then, the impacts of catalyst coating and microwave irradiation (solution temperature) on membrane permeability were carefully examined and interpreted by the Carman-Kozeny, Hagen-Posieulle and Boussinesq models. The removal and degradation efficiencies of PFOA via continuous filtration were evaluated under different operation conditions (e.g., w/o microwave irradiation, different flow rates and catalyst coating densities). Finally, degradation by-product formation was analysed to unravel degradation mechanisms of PFOA under this microwave-Fenton-like reaction. This hybrid filtration system is shown to enhance the degradation of refractory PFOA, whereas the physical adsorption and filtration both lead to insufficient removal.
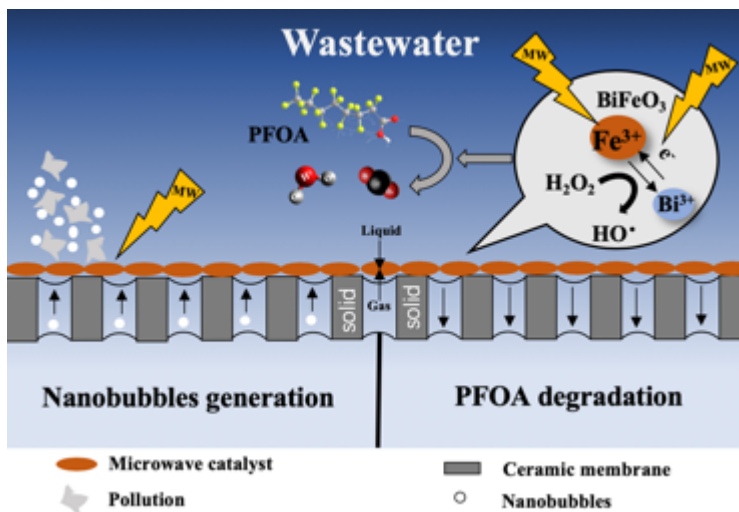
Figure 1.1 Schematic of degradation of PFOA in MW-Fenton-like process.
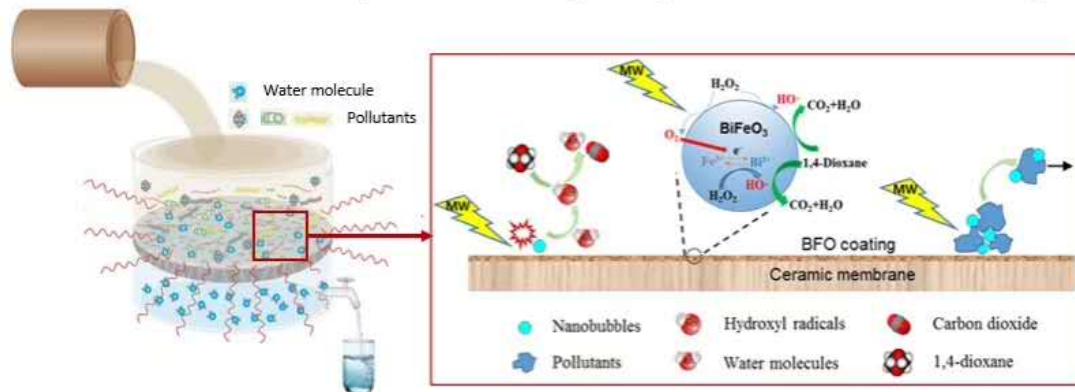
Figure 1.2 A patented process that utilizes microwave to catalyze surface reactions on ceramic membranes that promote degradation of pollutants.
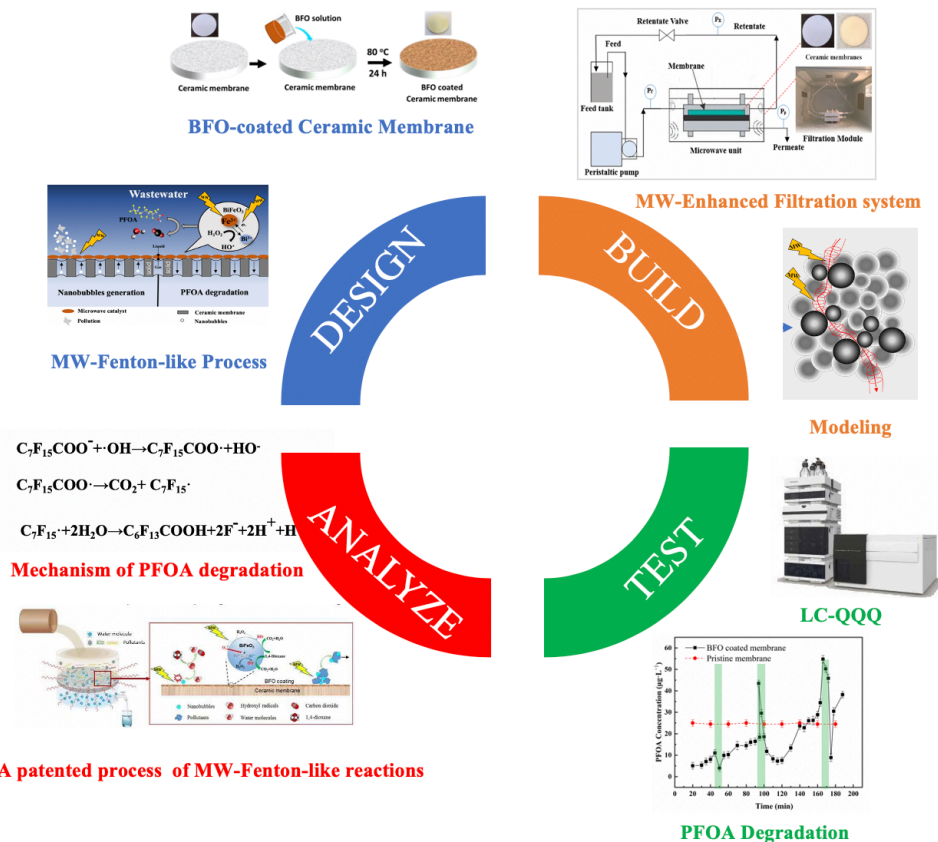
Figure 1.3 The Design-Build-Test -Analyze cycle for enhanced removal of PFOA via microwave-Fenton-reactive membrane filtration.

CHAPTER 2

MATERIALS AND METHODS

2.1 Materials

All chemicals used in experiment are analytical grade. Iron nitrate nonahydrate $(Fe(NO_3)_3 \cdot 9H_2O)$, bismuth nitrate pentahydrate $(Bi(NO_3)_3 \cdot 5H_2O)$, hydrogen peroxide (30%, w/w) were purchased from Sigma-Aldrich. Perfluorooctanoic acid (95%) was obtained from Alfa Aesar Chemicals (CAS NO. 335-67-1). PFAS species (50 ppm) (purchased from Wellington Lab (catalog# PFC-C-CS3). The Ammonium Acetate $(C_2H_7NO_2)$ and Methanol (CH_4O) are LC/MS grade purchased by Fisher Chemical. All solutions were prepared with deionized water with a Direct-Q® UV3 System (EMD Millipore, Bedford, MA, USA) over 18 M$\Omega \cdot$cm^{-1}.

2.2 BiFeO$_3$ (BFO) Synthesis

BFO catalyst was synthesized in a microwave-assisted hydrothermal method as reported previously [92]. Briefly, $Bi(NO_3)_3 \cdot 5H_2O$ (1 mM) and $Fe(NO_3)_3 \cdot 9H_2O$ (1 mM) in a stoichiometric rate (1:1 in molar ratio) were mixed with. NaOH solution (1 M) was then gradually added to the mixture with stirring for 15 min. Next, a microwave oven (300 W, 2.45 GHz, Sineo Microwave Chemistry Technology Co., Ltd, China) was used to irradiate the solution at 190 °C for 30 min. After that, the obtained black composite was separated by centrifugation and was washed at least three times with DI water and ethanol. Finally, a vacuum oven is used to dry catalyst powder for 12 h at 60 °C for later use.

2.3 Preparation of Catalyst Coated Ceramic Membranes

A flat-sheet ceramic membrane (47N014, Sterlitech Corporation, US) was used as a base support for catalyst functionalization as shown in **Figure 2.1**. This planar membrane is made of a zirconia/titania (Zr/TiO$_2$) coating on an alumina (α-Al$_2$O$_3$) supported with pore size of 5 nm (the approximate molecular weight cut off of 1kDa) /140 nm and an effective surface area of 17.34 cm^2. The inorganic and hydrophilic properties of these ceramic membranes provide great durability across a wide array of laboratory-scale microfiltration. The Zr/TiO$_2$ coating layers are inert to most corrosive chemicals, solvents, and extreme pH conditions.

Figure 2.1 Shape and model of the ceramic membrane.

    Bis-(3-[triethoxysilyl]-propyl)-tetrasulfide ((0.56%, w/w), w/w, in water) was used as a silane binder solution.[93] 30 mg BFO particles were added in this silane solution and ultrasonicated for 10 min.The ceramic membrane was soaked into BFO solution and placed in a vacuum oven at 80 °C for 24 h.(**Figure 2.2**) In this way, the functionalized ceramic membranes remained high permeate flux. The stability of BFO on membrane surface will be analyzed after the filtration experiments.
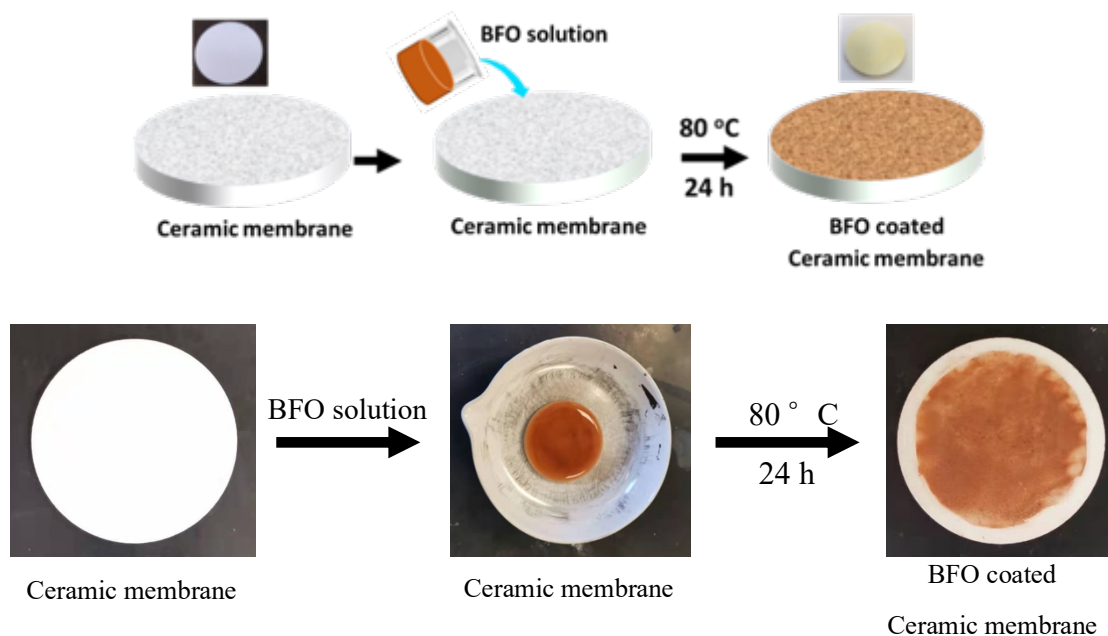
Figure 2.2 Schematic representation of the BFO-coated ceramic membrane preparation. Source:[89]

2.4 Characterization of Catalyst Coated Ceramic Membranes

FESEM was performed on a Hitachi S4700 F-SEM (Nissei Sangyo America, Gaithersburg, MD). Several attempts to obtain optimum imaging conditions resulted in selection of an electron energy of 5 kV. Lower kV settings did not have the required resolution; higher kV settings tended to penetrate into the particles too deeply, resulting in the loss of surface detail. Both lower SE(L) and upper SE(U) secondary electron detectors were used with a working distance ranging from 11.6 to 3 mm. The sample was prepared by sprinkling Fe onto a colloidal carbon covered aluminum stub. The loose, excess powder was blown off with an air gun.

AFM images of the uncoated and coated membranes were obtained using a Nanoscope IV Multimode Atomic Force Microscope (Digital Instruments Inc.), in ambient air in contact mode, which is ideal for examination of textured samples like ceramics. The tip

has a nominal radius of curvature of 20 nm with a height 2.5–3.5 μm and a side angle of 35°. Scans of 20 μm × 20 μm were taken at a scanning rate of ~0.2 Hz. the AFM Nanoscope software was used to obtain the Ra, RMS and PSD values. Quantitative information concerning the power spectral density (PSD), roughness (Ra and RMS) and cross-section analysis were obtained from the AFM images of the specimens.

2.5 Pure Water Permeability Using Pristine Ceramic Membranes

Permeability of coated membranes was assessed by the permeate flux, commonly expressed in units of litres per m^2 of membrane per hour (L m^{-2} h^{-1}, LMH), can be calculated by the Darcy's equation in **Eq. 1**:

$$J_w = \frac{V}{At} = \frac{TMP}{u(R_m + R_f)} = \frac{P_F - P_P}{u(R_m + R_f)} \qquad (2.1)$$

where J is the permeate flux (LMH), V is the permeate volume (L), A is the effective surface area of the membranes (m^2) and t is the time of the permeate collection (h), TMP is the trans-membrane pressures (Pa), which is the difference of the hydraulic pressure in the feed stream (P_F) and the hydraulic pressure in permeate stream (P_p). P_F was monitored by a pressure gauge (PEM-LF SERIES, WINTERS), while P_p was equal to the atmospheric pressure. μ is the dynamic viscosity of water at 25 °C (0.8937×10^{-3} N·s·m^{-2}), R_m is the background membrane resistance and R_f is the fouling layer resistance, which contribute to the total membrane hydraulic resistance (for clean water tests, $R_f = 0$).

The overall membrane porosity (ε) was determined by a gravimetric method, as defined in the following equation:[94]

$$\varepsilon = \frac{m_w - m_d}{\rho A L} \tag{2.2}$$

where m_w is the weight of the wet membrane (after immersed in water for 24 hours); m_d is the weight of the dry membrane; A is the membrane surface area (m^2), ρ is the water density (1×10^6 g·m^{-3}), and L is the membrane thickness (m).

To determine the changes of mean pore radius (r_m) of membranes, the Guerout–Elford–Ferry equation was employed:[95]

$$r_m = \sqrt{\frac{(2.9 - 1.75\varepsilon) \times 8\eta L Q}{\varepsilon A \Delta P}} \tag{2.3}$$

where η is the water viscosity (8.9×10^{-4} Pa s), Q is the volume of permeate water per unit time (m^3·s^{-1}), and ΔP is the operation pressure (3.5×10^4 Pa).

2.6 Modeling of Permeate Water Flux Under Different Temperatures

Three models are employed to demonstrate the temperature dependence of permeate flux on the pristine and catalyst-coated membranes.

(1) Hagen-Poiseuille Model (Cylindrical pores)

The Darcy's law gives the flow through a porous material as proportional to the pressure gradient $J_V = K(\Delta p / l_m)$ and, including explicitly the viscosity [96]:

$$J_V = \frac{k}{\eta} \frac{\Delta p}{l_m} \tag{2.4}$$

where J_v is the volume flow per unit of area (m^3·m^{-2}·s^{-1}), η is the viscosity of the fluid (Pa·s), Δp is the pressure drop (Pa), l_m is the thickness of active layer (m), and k is the multiplicative constant that depend only on the geometric properties of the porous membrane. If the membrane consists of cylindrical pores that are perpendicular to both the membrane surfaces, the Navier-Stokes equation can be solved, with the non-slipping

condition on the walls and incompressible flow, to obtain the Hagen-Poiseuille equation (2):

$$J_V = \frac{\varepsilon \cdot \Delta p}{8 \cdot \eta \cdot \tau \cdot l_m} \cdot r_p^2 \qquad (2.5)$$

$$k = \frac{\varepsilon}{8 \cdot \tau} \cdot r_p^2 \qquad (2.6)$$

where J_v is the volume flow per unit of area ($m^3 \cdot m^{-2} \cdot s^{-1}$), η is the viscosity of the fluid (Pa·s), Δp is the pressure drop (Pa), l_m is the thickness of active layer (m), ε is surface porosity (%), $\tau = l / l_m$ is a tortuosity factor (in many cases, $\tau = 2.5$), l is the pores length (m), r_p is pore radius (m). The overall membrane porosity (ε) can be determined by a gravimetric method as follows [94]:

$$\varepsilon = \frac{m_w - m_d}{\rho A L} \qquad (2.7)$$

where m_w is the weight of the wet membrane (after immersed in water for 24 hours); m_d is the weight of the dry membrane; A is the membrane surface area (m^2), ρ is the water density (1×10^6 $g \cdot m^{-3}$), and L is the membrane thickness (m).

(2) Boussinesq Model (Slit-like pores)

If slit-like pores ($H \times h$ rectangles with $H \gg h$) are considered, Eq. (2) must be substituted (without considering any border effects along h) by:

$$J_V = \frac{\varepsilon \cdot \Delta p}{12 \cdot \eta \cdot \tau \cdot l_m} \cdot h^2 \qquad (2.8)$$

$$k = \frac{\varepsilon}{12 \cdot \tau} \cdot h^2 \qquad (2.9)$$

where h is the width of rectangular channel; H is the length of rectangular channel.

(3) Carman-Kozeny Model (Capillary pores)

For inorganic membranes, the porous structure is assumed to be contributed by differently sized and closely packed spheres. The flux pathway is similar with capillary pores [97]. An equivalent hydrodynamic pore radius (r_p) is often assumed to be twice the cross-section area divided by the wet perimeter of cross-section, which leads to the Carman-Kozeny equation:[98] [99]

$$k = \frac{\varepsilon^3 \cdot D_{part}^2}{180 \cdot (1-\varepsilon)^2} \quad (2.10)$$

When Eq.(S7) is put into Eq.(S1), the relationship between pure water flux and membrane microsturcture parameters is written as

$$J_V = \frac{\varepsilon^3 \cdot D_{part}^2 \cdot \Delta p}{72 \cdot \eta \cdot (1-\varepsilon)^2 \cdot \tau \cdot l_m} \quad (2.11)$$

where D_{part} is the average particle diameter within the active layer of the membrane (m). ε is the volume porosity that may differ from the porosity within the surface layer.

Table 2.1 The Parameter of Water Flux Models

Flux model	Carman-Kozeny equation model:	Hagen-Poiseuille equation (non-slipping)	Hagen-Poiseuille equation (slip-like)
Equation	$J_V = \dfrac{\varepsilon^3 \cdot D_{part}^2 \cdot \Delta p}{72 \cdot \eta \cdot (1-\varepsilon)^2 \cdot \tau \cdot l_m}$	$J_V = \dfrac{\varepsilon \cdot \Delta p}{8 \cdot \eta \cdot \tau \cdot l_m} \cdot r_p^2$	$J_V = \dfrac{\varepsilon \cdot \Delta p}{12 \cdot \eta \cdot \tau \cdot l_m} \cdot h^2$
Known input parameter	η change with temperature. Δp =25855.35 Pa τ=2.5	η change with temperature. Δp =25855.35 Pa τ=2.5	η change with temperature. Δp =25855.35 Pa τ=2.5
Estimated input parameters	l_m (pristine)=20μm l_m (coated)=25μm	l_m (pristine)=20μm l_m (coated)=25μm	l_m (pristine)=20μm l_m (coated)=25μm

	ε (pristine)=50.9%	ε (pristine)=50.9%	ε (pristine)=50.9%
	ε (coated)=40%	ε (coated)=40%	ε (coated)=40%
	D_{part} (pristine)=100nm	r_p =70 nm	h =70nm
	D_{part} (coated)=120nm		
Output parameters	J_v	J_v	J_v

2.7 Preparation of Filtration System Under Microwave Irradiation

A commercial microwave oven (1250 W, 2.45 GHz, Panasonic Co., China) was used to irradiate a membrane filtration cell, which consists of a membrane holder, screen mesh, screws and nuts. All of these parts are made of Teflon (PTFE) that is nonpolar and thus does not absorb microwaves (transparent to microwaves). Thus, microwave can effectively pass through membrane housing and irradiate catalysts on membrane surface. The temperature of the filtration cell and solutions in the feed tank and pipes were measured with a Raytek MiniTemp MT4 non-contact infrared thermometer equipped with a laser pointer (Raytek Corporation Santa Cruz, CA, USA).

Two ceramic membranes with different BFO coating densities (1.6 and 2.7 $\mu g \cdot cm^{-2}$) were used in a dead-end filtration mode with the feed solution passing through the membrane. A modified syringe pump was used to transfer the solution from a PFOA (50 $\mu g \cdot L^{-1}$) solution and the hydrogen peroxide (30 mM) solution at different flow rates (1.25-7 mL·min) as illustrated in **Figure. 2.3**. As the PFOA and H_2O_2 solutions were mixed in a volume ratio of 1:1 at a tee, the actual concentration of PFOA entering the filtration unit was 25 $\mu g \cdot L^{-1}$. This initial PFOA concentration was chosen because the typical PFAS concentration in wastewater is generally at the ppb to ppt level. Before applying MW, the

filtration system was run for 30 min to reach a stable permeate water flux. The contributions of PFOA removal from physical separation (size exclusion and sorption or chemical binding with ceramic membrane) and MW-Fenton-like degradation were differentiated and quantified by switching microwave irradiation "on" or "off". Microwave was provided at 125 watts with 5 min-on/5 min-off cycles. Transmembrane pressure (TMP) and permeate temperature (near the permeate outlet port) were recorded during the filtration process. The permeate samples were taken during each 5 min to measure the PFOA concentrations. After each filtration experiment, the pipes in the filtration system were washed by DI water for 30 min, and BFO coated ceramic membrane was immersed by DI water excessively. The removal ratio of PFOA was calculated by:

$$R(\%) = \frac{C_0 - C}{C_0} \times 100\% \tag{2.12}$$

where R is the removal rate of PFOA, C_0 and C are initial and instantaneous concentrations of PFOA ($mg \cdot L^{-1}$), respectively.

Based on the above experiment condition, we conducted a recycle experiment to test the sustainability of PFOA degradation by the MW-enhanced membrane filtration system. Before microwave irradiation, the experiment process is the same as above. After microwave irradiation, the effluent will continuous flow back to the PFOA feed tank to achieve the recycle filtration system. Based on the filtration system volume (approximately 20ml) and permeate flux (43LHM), we set 20 minutes as a cycle. In order to ensure sufficient hydroxyl radicals, hydrogen peroxide is continuously pumped into the system throughout the filtration process.
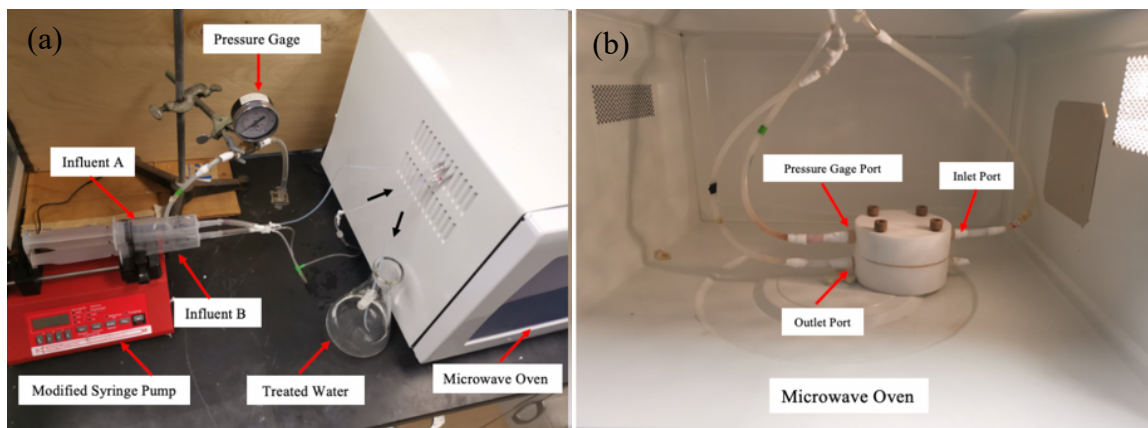
Figure 2.3 (a) The PFOA (50 μg·L^{-1}) solution and the hydrogen peroxide (30 mM) solution were pumped into filtration system by modified syringe pump. (b) The dead-end filtration mode in the microwave oven.

2.8 Analysis Method

An Agilent 6470A triple quadrupole LC/MS system was used to detect the concentrations of PFOA and intermediates (C$_2$ ~ C$_7$) during degradation based on USEPA Method 537. C18 column (Agilent poroshell 120 EC, 50 × 3 mm, 1.8 μm) was used for separation at 40 °C using a mobile phase of solvent A (5 mM ammonium acetate in distilled water) and B (5 mM ammonium acetate in 100% methanol). The injection volume of each sample is 5 μL with a flow rate of 0.5 ml·min^{-1}. All samples, standards and blank were filed by 0.22 μm syringe filter (Basix Syringe Filters, PES, Sterile). The compounds were analysed by an electrospray negative ionization mode. The mode of multiple reaction monitoring with −4.5 kV of ion spray voltage was used to perform the analysis . The fluoride ion in the solution was analysed by Metrohm 881 Compact Ion chromatography (IC) Pro coupled with a Metrosep A Supp 5-250 column.

NPOC/TN measurements were obtained using Shimadzu TOC-L CSH/CSN Total Organic Carbon Analyzer and Shimadzu TNM-L Total Nitrogen Measuring Unit. Data were evaluated with TOC-Control L software (ver. 1.04.). Alkaline thermal water sample

in a 1:10 dilution is sparged with HCl to remove inorganic carbon. Then the water sample is injected onto a combustion column packed with platinum-coated alumina beads held at 720°C. Non-purgeable organic carbon (NPOC) compounds are combusted and converted to CO_2, which was detected by a nondispersive infrared detector (NDIR at 65°C). Sparge gas flow was 81.0mL/min. The supply gas pressure was 189.7kPa and the carrier gas (synthetic air) flow 150.0mL/min^{-1}.

2.9. Quality Control and Quality Assurance.

2.9.1. Data Quality and Determine Reporting Limits For LC-QQQ analysis, several calibration verification checks were performer after calibration (Agilent 6470 Triple Quad LC/MS), every 15-20 samples, and at the end of analysis. The spectra generated in the LC-QQQ were inspected to check for spectra interference. The proficiency of the analysis is determined by the observation of their QA/QC performance. This includes factors such as: the relative standard deviation (RSD) on replicates of unknowns, external check sample results, their technique for standard and reagent preparation and ability to follow standard laboratory procedures.

a. Precision: The precision of the analysis will be examined using the relative percent different of duplicate samples, with the RSD. The RSD can be calculated as follows: [100]

RSD = 100[(X1-X2)/X1]
where:
X1 = First observation of unknown X
X2 = Second observation of unknown X
RSD values of 15% will be acceptable. If RSD > 15%, samples will be reanalyzed with a lower dilution when possible.

b Accuracy: The accuracy of the measurements will be tested with a CCV every 15-20 samples. In addition, blind standards run as samples with known concentrations will be

placed between samples as a secondary quality control check for accuracy. We will consider the instrument is out of accuracy when the measured value is deviated of the standard deviation more than 20%.

c Representativeness: Each experiment had a specific sampling protocol prior to conducting any sampling, which were reviewed by QA officer, with the objective of ensuring the representativeness of the samples. The number of the collected sample and the sampling strategy will depend on the specific experiment duration and objective. Representativeness within the sample will be achieved by homogenization of each sample through thorough mixing before the analyses.

d. Comparability: Comparability of the data was obtained by following the same operational procedure for sample collection, processing and analysis.

e. Completeness: It is the responsibility of the project to ensure that: (1) all the samples required per the sampling protocol are collected; (2) that the samples are properly labeled and preserved; (3) that all the quality control checks are included; (4) that all the information required for sample preservation and preparation is completed; (5) that the samples are analyzed and the results are received within a reasonable amount of time; (6) that the analysis has passed all the quality control checks within 20% of error; (7) that if there is any problems with the analysis is recorded and communicated; (9) that the results generated from the analysis are stored and saved.

2.9.2. Calibration Curve and LOD   The LC-QQQ instruments as shown in **Figure 2.4** was calibrated prior to any analysis. The calibration curves had at least 5 points plus a blank in the curve, ranging from the lowest to the highest expected concentrations of the samples to be analyzed (based on historical knowledge of the area, research estimation). If the method required validation (for new methods or high-priority samples), another calibration curve (standards as samples) might be repeated at the end of the analysis, for other measurements such as pH and conductivity, instruments are calibrated according

to manufacturer's instructions. In general, the calibration will be accepted if the R (correlation coefficient) is > 0.99.

Figure 2.4 Agilent 6470A LC-QQQ instrument.

The calibration curves of PFBS, PFHxA, PFHpA, PFHxS, PFOA, PFOS, PFPeA are made following LC-QQQ protocol (**Figure 2.5**). The coefficients of determination (R^2) for all eight calibration curves were larger than 0.99. The limit of detection (LOD), according to the EPA 537.1 are depends on the system sensitivity using the following equation:

$$\text{LOD} = \frac{S_b \times k}{m} \qquad (2.13)$$

where k is a factor with the value of 3, S_b is the standard deviation of the blank and m is the slope of the calibration graph in the linear range. The LOD for the 8 PFAS compounds are shown in the **Table 2.2**.
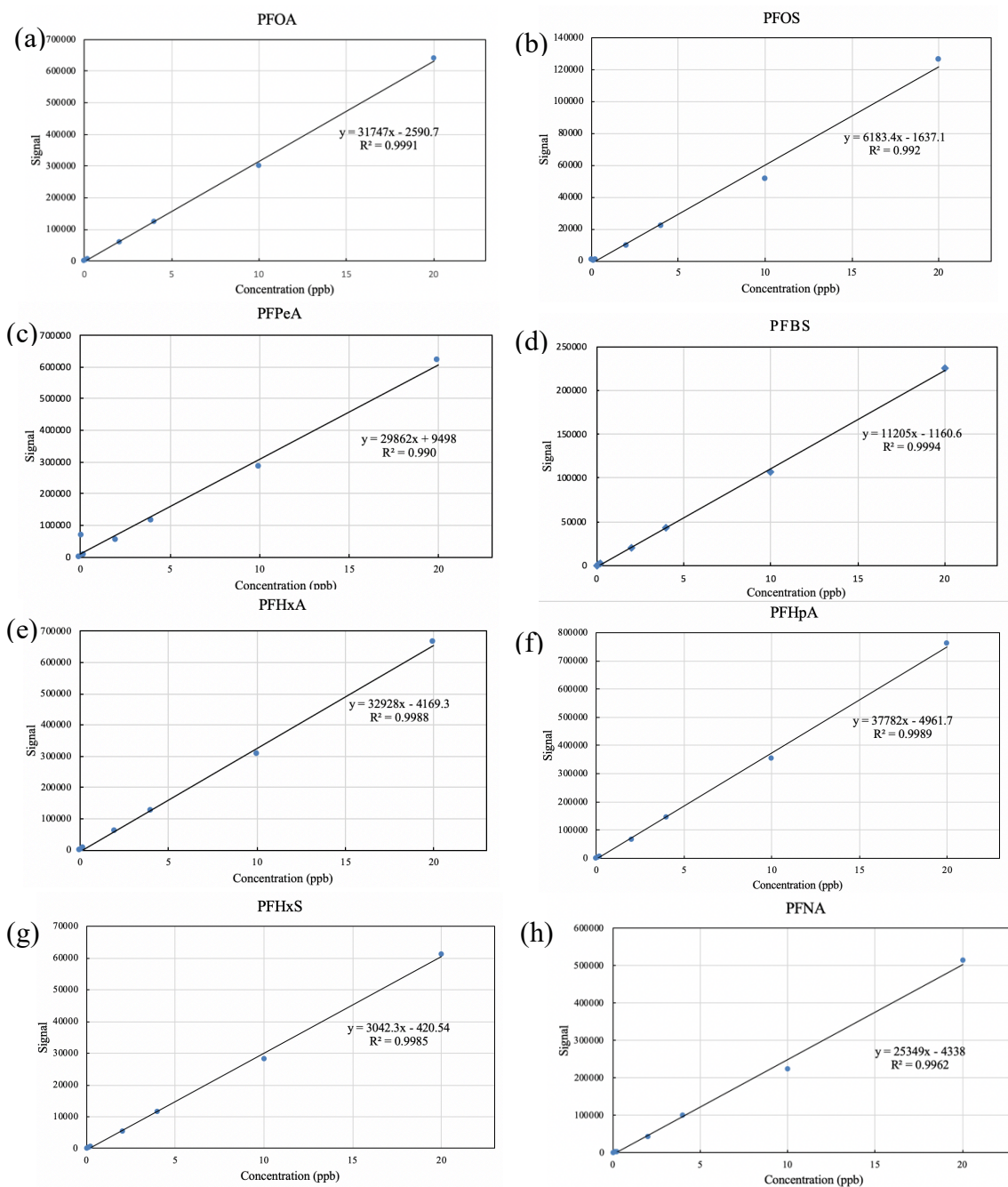
Figure 2.5 The calibration curves of PFBS, PFHxA, PFHpA, PFHxS, PFOA, PFOS, PFPeA and PFNA (a)-(h).

Table 2.2 The LOD of PFBS, PFHxA, PFHpA, PFHxS, PFOA, PFOS and PFNA

	Name	Molecular Fomular	LOD (ppb)
1	PFOS	$C_8HF_{17}O_3S$	2.41

2	PFOA	$C_8HF_{15}O_2$	0.81
3	PFNA	$C_9HF_{17}O_2$	1.67
4	PFBS	$C_4HF_9O_3S$	0.66
5	PFHpA	$C_7HF_{13}O_2$	0.90
6	PFHxS	$C_6HF_{13}O_3S$	1.03
7	PFHxA	$C_6HF_{11}O_2$	0.94
8	PFPeA	$C_5HF_9O_2$	3.2

2.10 The Quality Indicator of Raw Water

2.10.1 Total Phosphorus (TP) 5 ml sample persulfate powder and reagent are mixed in a digest via. Then, the vial is heated for 30 min at 150 °C. After Cool down to room temperature, the vial is added 2 ml 1.54 N NaOH solution and mix well. Next, a PhosVer 3 powder reagent is added to vial. After waiting for 2 min, UV spectrophotometer is used to detect the TP content at 880 nm.

2.10.2 Total Nitrogen (TP) Add 1 persulfate powder reagent and 2ml sample to one hydroxide digest vial. Then, the vial is heated for 30 min at 105 °C. After Cool down to room temperature, the vial is added 1 reagent A powder and mix well. After 3 min, 1 reagent B powder is added to the vial with 15 second shaking. Then waiting for 2 min and transfer 2 ml solution to one Reagent C vial. Finally, the solution is measured Abs at 410 nm.

2.10.3 Ammonia 10 ml sample and 1 salicylate powder reagent are mixed in a 15 ml centrifuge tube. Then, 1 cyanurate powder reagent is added to the tube after 3 min. After well shaking and 15 min waiting. UV spectrophotometer is used to detect the Ammonia content at 655 nm.

2.10.4 Nitrite   Add 10 ml sample and 1 NitraVer 3 powder reagent to a 15 ml centrifuge tube. Swirl to dissolve the reagent. Measure Abs at 507 nm after waiting for 20 min.

2.11. PFAS Extraction Procedure and LOD Determination

2.11.1 PFAS Standard Sample and Cartridge SPE Preparation

The procedure of extraction of PFAS is performed following with EPA 537.1. The mixed 50 ppm standard PFAS. diluting with DI water to 250-mL, 10 ppt which is used for extraction efficiency by solid-phase extraction (SPE). Before the extraction with SPE cartridge, pre-condition procedures with clean-up and conditioning are necessary with the following steps as shown in **Figure 2.6**. First, rinse each cartridge with 15-mL of methanol and following with 18-mL of reagent water. The spiked aliquot (methanol and water) must be always above the top surface of the packed cotton filter to maintain good cartridge-liquid immersion. After that, closing the valve and adding 4-mL of reagent water to each cartridge to keep cartridge from drying. When the clean-up and conditioning are completed, capping the cartridge with parafilm, filling sample to the cartridge then turning on the vacuum.
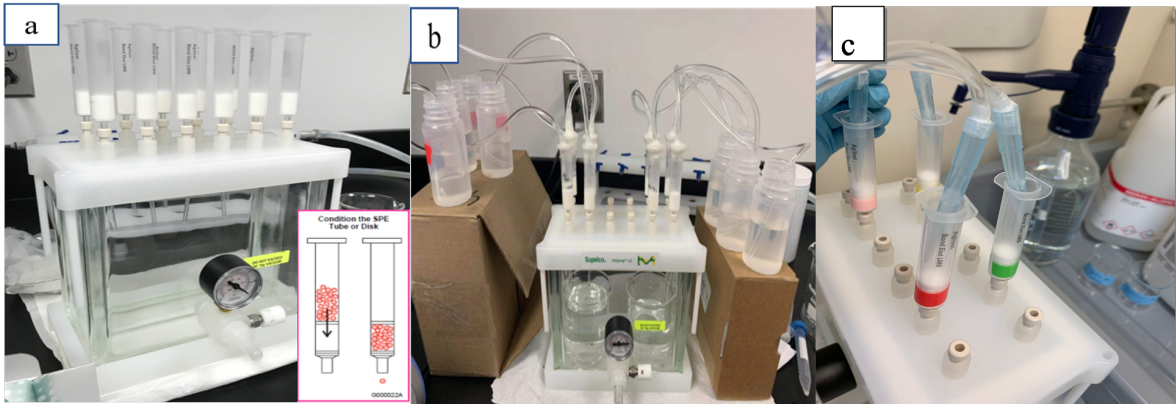
Figure 2.6 SPE cartridge pre-condition procedures. (a) SPE cartridge and the manual clean-up and conditioning process. (b) Water sample injection into the conditioned cartridge. (c) air/nitrogen purging.

2.11.2 Analyzed Sample Extraction and Elution Processes

Figure. 2.7 shows the schematic of extraction and elution processes within the SPE cartridges. The samples (250-mL) are added to the cartridges at a flow rate 10-15 mL·min^{-1} via transfer tubes. After each entire sample has passed through the cartridge, turn off the flow control valve and rinse the sample bottle with 7.5-mL reagent water twice. Air or nitrogen is purged through the cartridge for 5 minutes at vacuum pressure of 10-15 in. 254-380 mm. Hg. In the sample elution process, turn off vacuum and rinse the sample bottles with 4-mL of methanol, which was then pipetted to the cartridges to elute the extracted PFAS by gravity twice as shown in **Fig. 2.7a**. Concentrating the extract by nitrogen purging within the heated water bath (60-65°C) to remove all the water/methanol mix (**Fig. 2.7b**). Finally, adding 96:4% (vol/vol) methanol: water solution into 15-ml PP conical tube to reach a final volume of 2 ml, which is then subjected to the LC/QQQ analysis.
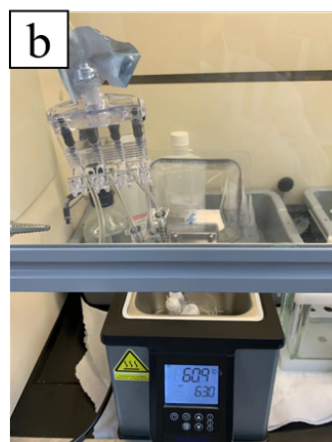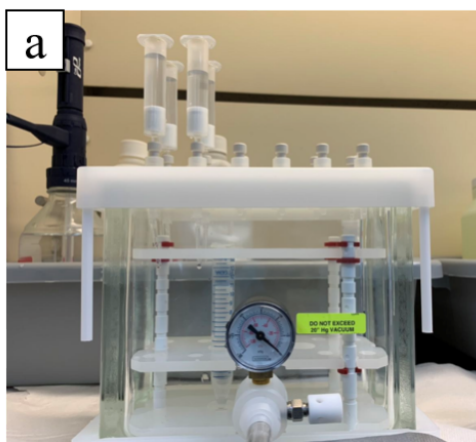
Figure. 2.7 Elution and extraction processes with (a) sample extraction and (b) water and methanol removal.

CHAPTER 3

RESULTS AND DISCUSSION

3.1 Characterization of Functionalized Ceramic Membranes

3.1.1 SEM and EDX Imaging.

The morphologies of pristine membrane, low BFO coated membrane (1.6 µg·cm^{-2}) and heavy BFO coated membrane (2.7 µg·cm^{-2}) are compared in **Figure 3.1**. It can be observed that the surface of pristine ceramic membranes contains pores with hundreds nanometer, which is consistent with the reported pore size of 140 nm by the manufacture. The EDX data (**Figure 3.2**) also showed that the pristine ceramic membrane exhibits a uniform three-dimensional structure with a thin zirconia/titania (Zr/TiO$_2$) coating on the top surface. **Figure 3.1 (b)** and **(c)** compared the coated result between low and heavy coated membrane and shows that BFO has a bead structure with a dimension of 5-20 µm while the magnified image showed that these spheres were consisted with numbers of cubic particles. [101] For the BFO/Ceramic membrane, the holes of the ceramic membrane coexist with many irregularly shaped particles. The EDX spectra (**Figure 3.2**) also confirmed the existence of titanium, zirconium, aluminum, oxygen, bismuth and iron elements in BFO/Ceramic membranes. **Figure 3.1 (d)** showed the structure of BFO coated membrane in cross-sectional images, consisting of α-Al$_2$O$_3$ supporter, Zr/TiO$_2$ layer and BFO coated layer. The SEM and EDX analysis proved that the ceramic membranes have been coated with BFO particles on the membrane surface.
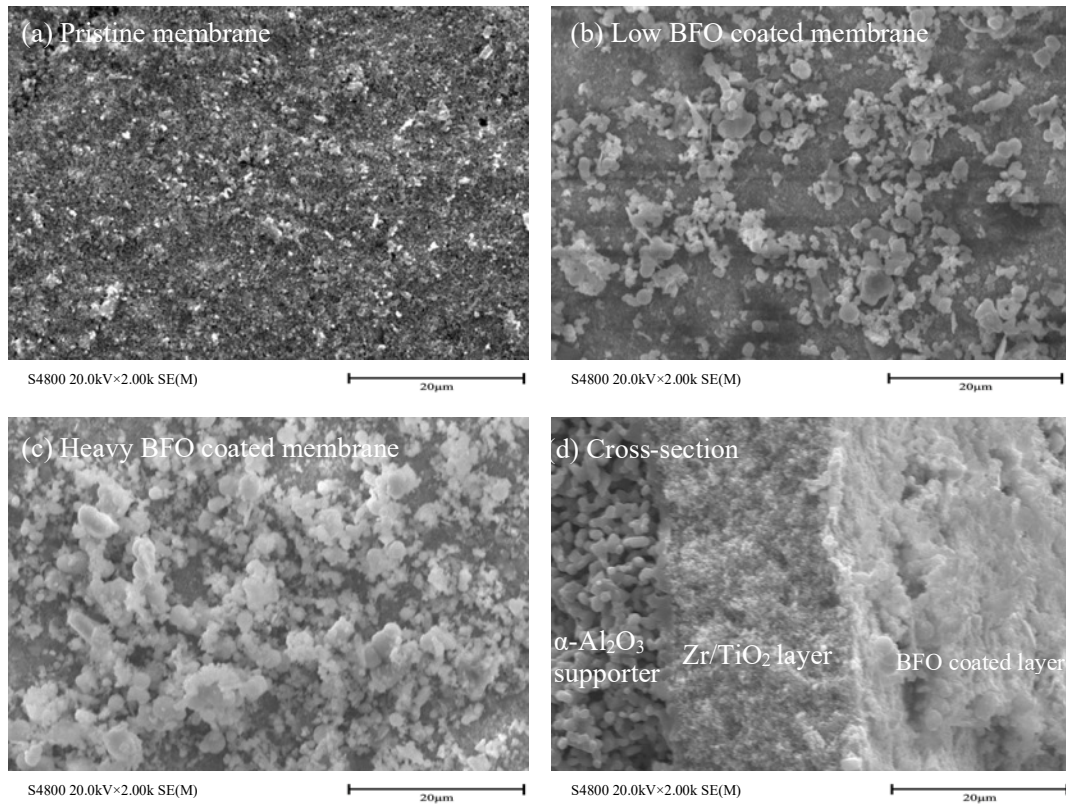
Figure 3.1 (a) Pristine membrane, (b) Low BFO coated membrane, (c) Heavy BFO coated membrane and (d) Cross-sectional images of BFO coated membrane.
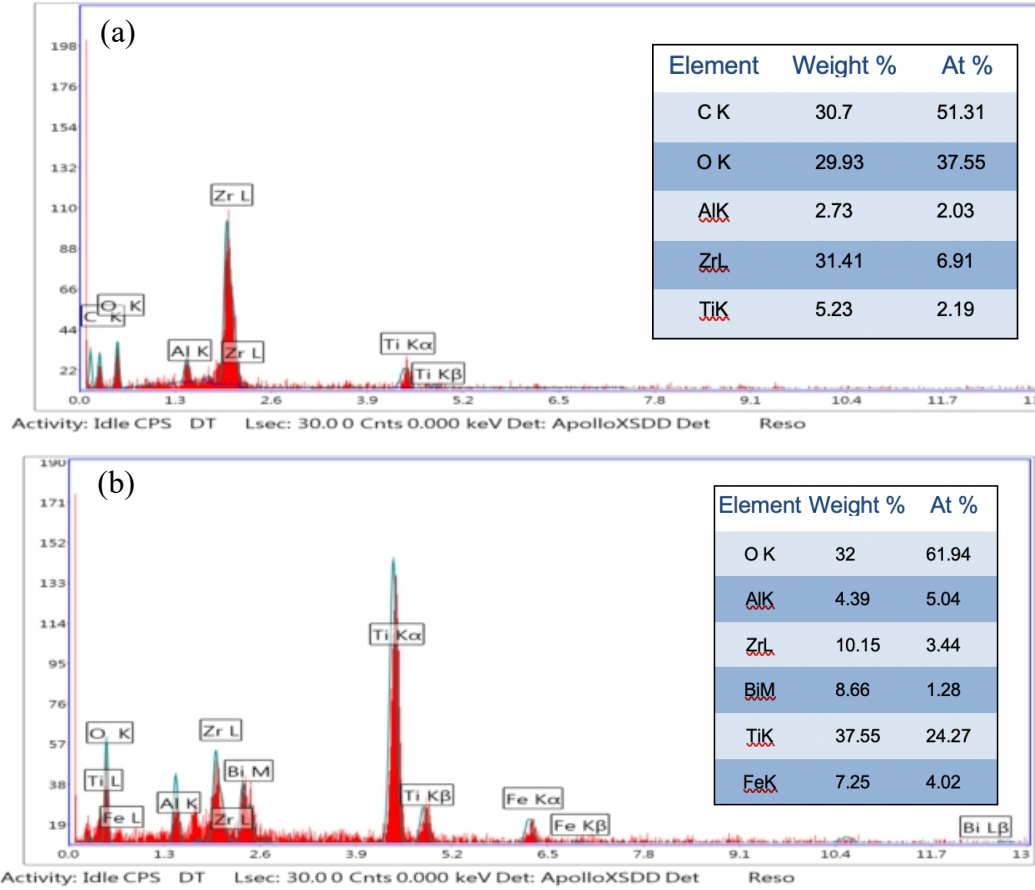
Figure 3.2 EDX analysis of (a) pristine membrane and (b) BFO coated membrane.

3.1.2 AFM Imaging.

AFM analysis provided data on the surface morphology and surface roughness. The manner in which these properties correlate with the surface porosity and filtration performance provide insight into the structure of the filtration membrane. The surface roughness from AFM measurements can be correlated to the grain size found using SEM. **Figure 3.3(a)–(f)** shows AFM 2D and 3D images of pristine membrane, low BFO coated membrane and heavy BFO coated membrane. For each AFM image, the area in view represents a 20 μm × 20 μm square. the surface of pristine membrane (**Figure 3.3(a)**) shows a relatively flat surface of pristine membrane with the flat featureless regions of

~506.9 nm (±0.2) height. With BFO coating (**Figure 3.3 (c)-(f)**), the surface of membrane from flat featureless regions of ~0.3µm (±0.2) height to more sharp surface features of ~2.2 µm (±0.2) height. Comparing the AFM imaging of low coated membrane, the heavy coated membrane presents a denser catalysts distribution.
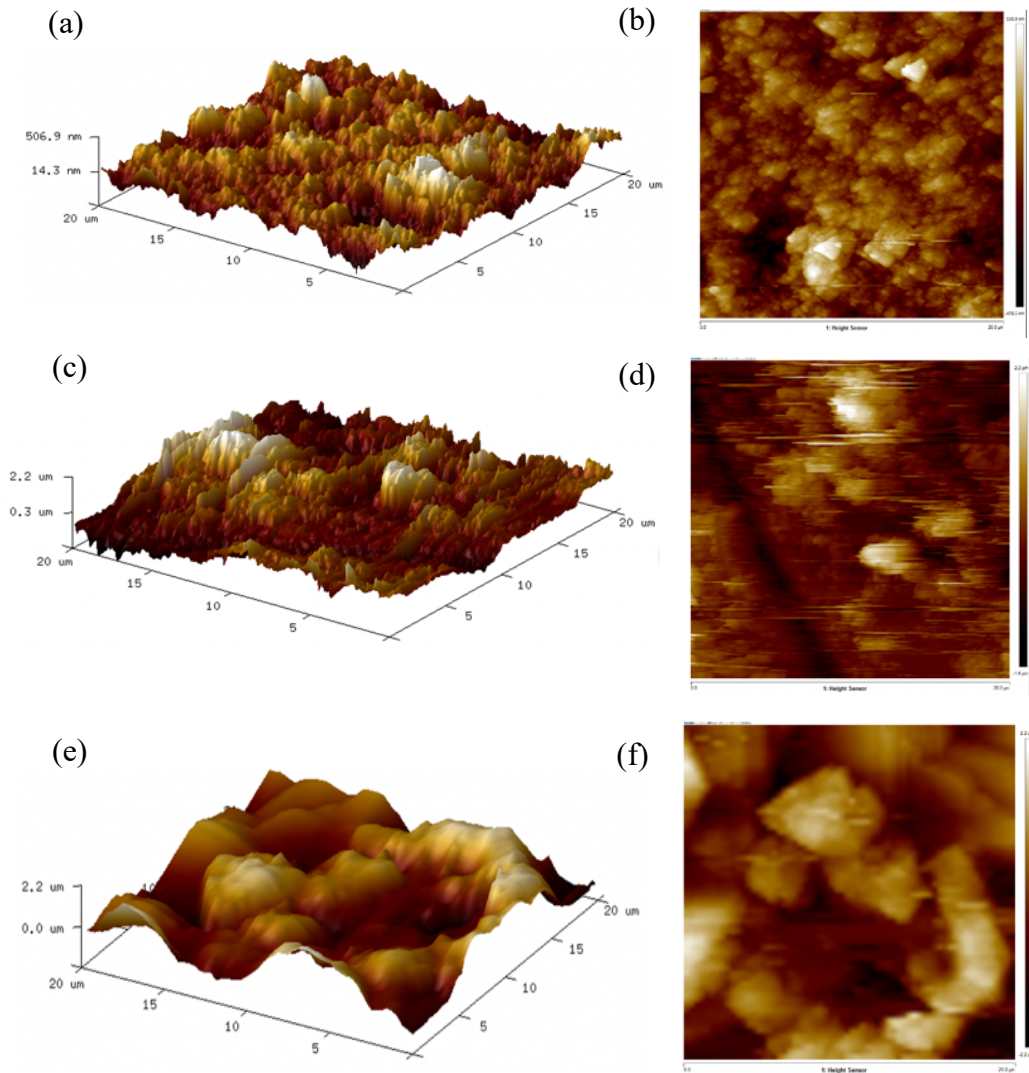
Figure 3.3 AFM 3D and 2D images of pristine ceramic membrane (a)-(b), low BFO-coated membrane (c)-(d), and heavy BFO-coated membrane (e)-(f).

The root mean square (RMS) roughness, Rq, was determined by AFM for the three membrane samples based on surface morphology mapping. Moreover, the one dimensional Power Spectral Density (PSD) was employed to determine the fractal dimensions [102]. The slope (m) fitted by the double-log plot of PSD versus the space frequency in **Figure 3.4** can be used to calculate the fractal dimension (D) using **Eq. 3.1** [103]:

$$D = (5 - m)/2 \tag{3.1}$$

The slope of the plots and the corresponding fractal dimensions (D) are both summarized in **Table 3.1**. A fractal dimension D of 1 means that the surface is fundamentally bidimensional or 2D, whereas a fractal dimension close to 2 would correspond to a 3D interface [104]. Clearly, the pristine membrane's surface structure is close to 2D, whereas the two catalyst-coated membrane have a 3D surface structure.
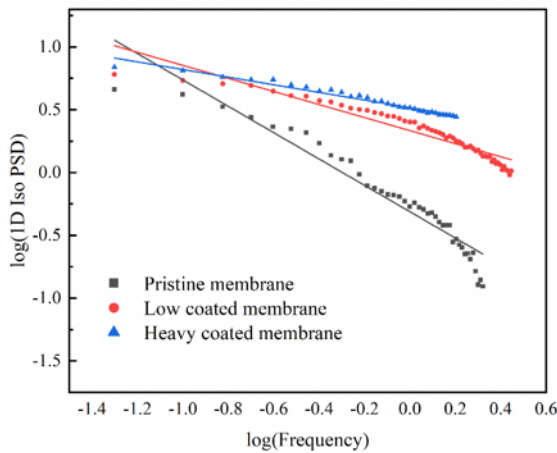
Figure 3.4 One-dimensional power spectral density (1D-PSD) vs. spatial frequency plots of pristine, low coating and heavy coating membranes.

Table 3.1 Roughness, Slope and The Corresponding Fractal Dimensions

	Roughness (nm)	Slope	Fractal dimensions
Pristine membrane	128 ± 15	-1.10 ± 0.1	1.95 ± 0.05
Low BFO-coated membrane	509 ± 15	-0.52 ± 0.1	2.24 ± 0.05
Heavy BFO-coated membrane	691 ± 15	-0.3 ± 0.1	2.35 ± 0.05

3.2 Flux Evaluation on Ceramic Membranes with/without BFO Coating

Figure 3.5 shows the clean water flux under various TMPs for ceramic membranes before and after catalyst coating at ambient room temperature. The permeate fluxes for coated membranes are lower than the uncoated ceramic membranes, due to the partial blockage by the coated catalyst [105]. However, the maintenance of permeability and abandence of reaction sites are predicted to be achieved by the mesoporous of BFO coated layer with large specific surface area. Based on the Carman and Kozeny equation [106], the porosity (ε) and pore size (d_h) of catalyst coated layers are in proportion to the catalyst particle diameter (500 to 550 nm). Thus, porous structures formed by the interstices between catalyst particles are able to allow for flux permeation. The Darcy's equation (**Eq.2.1**) was used to express the permeate flux (L m^{-2} h^{-1}, LMH) under different TMPs. The water permeability for the pristine ceramic membranes with a nominal pore diameter of 0.14 μm was reduce from more than 50.0 LMH·psi^{-1} to 39 and 43 LMH·psi^{-1} after heavy and low catalyst coating respectively, indicating that the membrane pore blocking by catalyst particles was acceptable. Furthermore, the inherent membrane resistance (R_m) for the pristine ceramic membranes increased from 5.72×10^{11} m^{-1} to 8.57×10^{11} m^{-1} and 9.59×10^{11} m^{-1} after

low and heavy catalyst coating respectively. Previously, Guo et al. reported similar observations that heavy surface coating of TiO_2/ZrO_2 catalysts increased the membrane resistance [107].
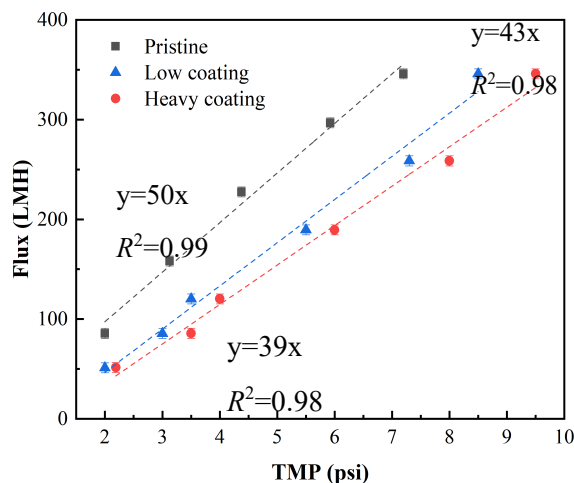
Figure 3.5 Pure water permeability of pristine and BFO-coated ceramic membranes. Low and heavy coating refers to coating densities of 1.6 and 2.7 $\mu g \cdot cm^{-2}$.

Water permeation of the modified membranes was monitored and compared with the pristine ceramic membrane. **Figure 3.6a** shows that the pure water permeability for both the pristine and BFO-coated ceramic membranes was enhanced almost twice under MW irradiation. However, no significant difference in water permeability was found between pristine and modified membranes. The elevated water permeability could be primarily attributed to the increasing water temperature (from 23±2 °C to 56±4 °C), which may alter the liquid viscosity and enhance the membrane flux. The increased flux under high temperatures was also reported in previous studies [108-110]. We did the control experiment with mildly heated water (60±5 °C) as the feed. The results (**Figure 3.6**) show that the water permeability was higher than that with the feed of room temperature (23±2 °C). Thus, a normalized flux at 25 °C was calculated to eliminate the influence of temperature on the membrane flux. **Figure 3.6b** shows that the normalized fluxes were similar under different

MW power levels, confirming that the increased water permeability was solely due to the elevated temperature caused by MW irradiation.
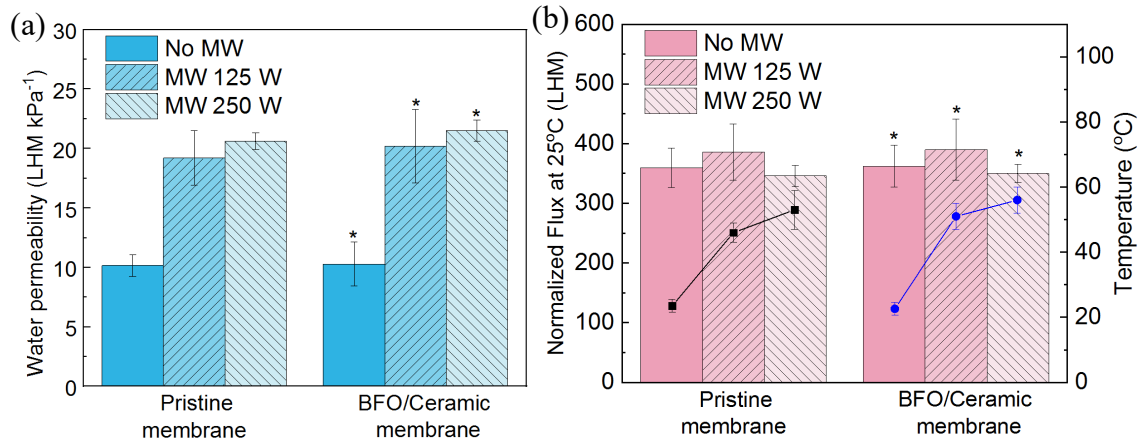
Figure 3.6 Pure water permeability, and normalized flux at 25°C of pristine membrane and BFO-coated ceramic membrane.

Source:[89]

3.3 Modeling of Relationship Between Water Flux, Viscosity and Permeability Parameters of Ceramic Membrane

Figure 3.7 shows that the permeate water fluxes of pristine and catalyst-coated membranes under different feed solution temperatures. Both two membranes had increased water fluxes consistently at increasing solution temperatures. The permeate fluxes of pristine membrane (**Figure 3.7a**) are greater than the coated membrane (**Figure 3.7b**) because the effective pores may be reduced by the catalyst coating. To further interpret the data, three flux models, Carman-Kozeny model, Hagen-Posieulle model and Boussinesq model, which assume that the flux pathway is similar with capillary pores, slit-like pores and cylindrical pores, respectively, were used to calculate the water fluxes under different temperature. The model equations and the used parameters are shown in **Table 2.1**. Among three models, the Carman-Kozeny model appears to generate the fluxes that are close to the experimental data. The Carman-Kozeny model assumes that a porous membrane is

formed by differently sized and closely packed spheres, which could be close to our ceramic membrane properties.

It is reported that the Carman–Kozeny (C–K) equation for an aggregate cake to predict the permeate flux by the structure parameters of a cake layer such as mean particle size, thickness, and voidage. The Hagen–Poiseuille (H–P) equation was also used to depict the pressure drop in the viscous fluid flow, but the essential separation mechanism of ceramic membranes based on microstructure parameters was hardly reported. Compared with the filtration cake, ceramic membranes sintered at a high temperature had a more complex porous microstructure. [99] In addition, Li et al indicated that Carman-Kozeny and Hagen-Posieulle model can both explain the experimental data when the membrane pore sizes are 500 and 800 nm [99]. However, the variation of water flux on ceramic membrane with a pore size of 100 nm was better predicted by the Carman-Kozeny model.
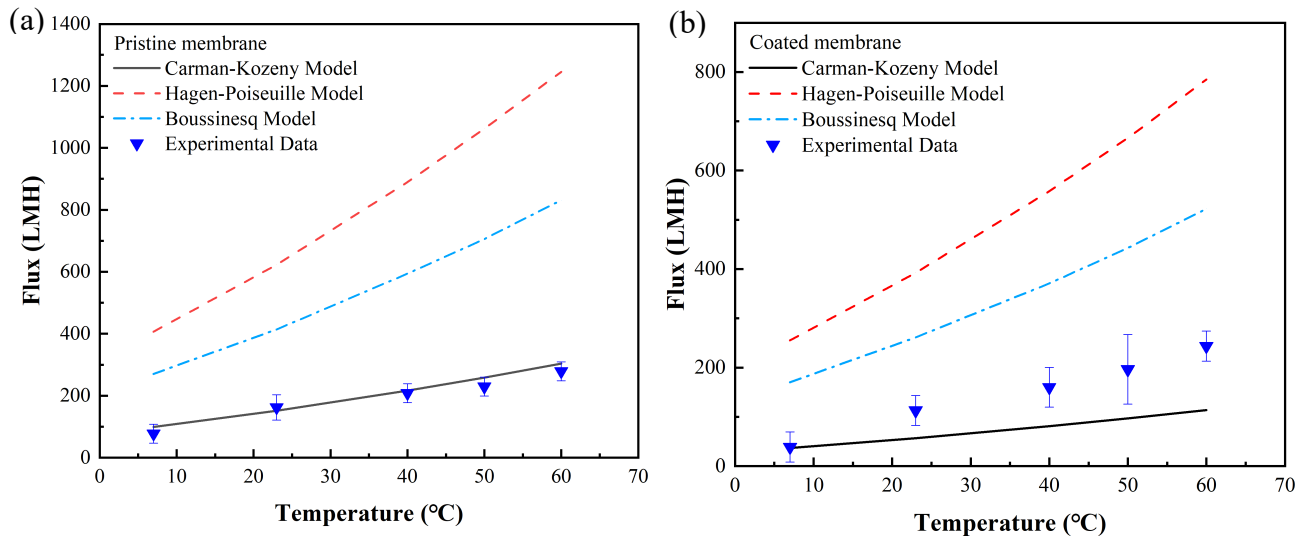
Figure 3.7 Permeate water flux of (a) pristine membrane and (b) BFO-coated membrane at different feed solution temperatures and comparison with the three model prediction.

3.4 Degradation Performances of PFOA by BFO Coated Membrane Filtration

3.4.1 Effect of Adsorption in Pristine and Coated Membrane

Ceramic membrane due to its selectivity, rejection, high temperature resistance and antifouling capability was tailored by anchoring of BFO catalysts. However, **Figure 3.8** shows that approximately 2% of PFOA was removed by the pristine ceramic membrane, which indicates that the contribution from the size exclusion or membrane surface adsorption was negligible. By contrast, when the ceramic membrane coated with BFO catalyst, the effect of PFOA adsorption was obviously manifested in the dropped PFOA concentration in the permeate that was lower than the initial concentration of 25 $\mu g \cdot L^{-1}$ in the initial filtration phase. Previous studies showed that BFO catalyst are a highly efficient adsorbent for removal of dyes from aqueous solution. [111-113] For example, the maximum adsorption capacities of RhB on BFO adsorbent can be reached to 11.9 $mg \cdot g^{-1}$ when pH of RhB solution was adjusted to 4.00.[113] And nearly 80% of the initial MO concentration of 2.5×10^{-5} M were captured by the $BiFeO_3/\alpha\text{-}Fe_2O_3$ core/shell composite particles within 5 min at an acidic pH of 5.2.[111] In addition, Shang et.al proved that PFOA was dissociated as anionic form while the surface charge of the $Pb\text{-}BiFeO_3/rGO$ was positive which promote the electrostatic attraction between them in the adsorption and degradation process.[114]
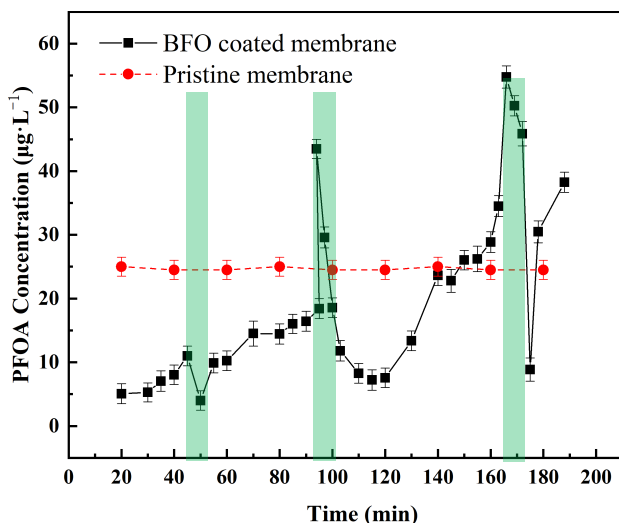
Figure 3.8 PFOA concentration changes in three consecutive round of filtration tests by using pristine and BFO coated membrane. The green bars indicate the operation of microwave irradiation during filtration, whereas other areas were operated without microwave irradiation and under filtration only. The initial spiked PFOA conentration: 25 $\mu g \cdot L^{-1}$; the microwave intensity: 125 watts (7.2 watt·cm^{-2}); the cataslyt coating density: 2.7 $\mu g \cdot cm^{-2}$; and the permeate flux: 43 LMH.

3.4.2 Effect of Microwave Irradiation

Figure 3.8 shows the degradation kinetics of PFOA in three consecutive cycles of filtration. Without microwave irradiation (0 min – 45 min), the PFOA concentration progressively increased as the adsorption reached equilibrium and PFOA started to penetrate the membrane filter. After the microwave irradiation started at 50 min as indicated by the green bar, the PFOA concentration was rapidly reduced, as the microwave-assisted Fenton-like reaction on BFO-coated membrane may enable the PFOA degradation. Once the microwave was turned off, the concentration of PFOA quickly elevated. This enhanced degradation under microwave was repeatedly observed in the second and third applications of microwave irradiation. Without microwave irradiation, we observed an incremental increase of the PFOA concentration due to the desorption or leakage of the adsorbed PFOA from the membrane or catalyst. The measured concentration of PFOA was even higher

38

than the spiked concentration (25 $\mu g \cdot L^{-1}$), probably because the accumulated PFOA was flushed out and caused a sudden increase of PFOA in the permeate. Additionally, the transmembrane pressure (TMP) increased from 6.1 psi to 14 psi due to the membrane fouling that is likely attributed to the accumulation of surface adsorbed PFOA and other degradation by-products. The microwave-assisted Fenton-like reaction contributed to approximately 65.9% of PFOA that was removed this reactive membrane filtration.

3.4.3 Effect of Permeate Flux

Permeate flux determines the hydraulic retention time and the organic pollutant loading rate on the membrane surface, which affect the performance of the pollutant degradation [115, 116]. **Fig. 3.9a** indicates that under a high permeate flux of 242 LMH (retention time of 21s), the PFOA concentration remained almost unchanged with or without microwave irradiation. However, under a low permeate flux of 43 LMH (retention time of 2 min), an incremental increase of the leached PFAS concentration was observed presumably due to the adsorption effect. Under microwave irradiation, the degradation of PFAS was apparently enhanced, probably because PFOA had sufficient time for catalytic reactions.
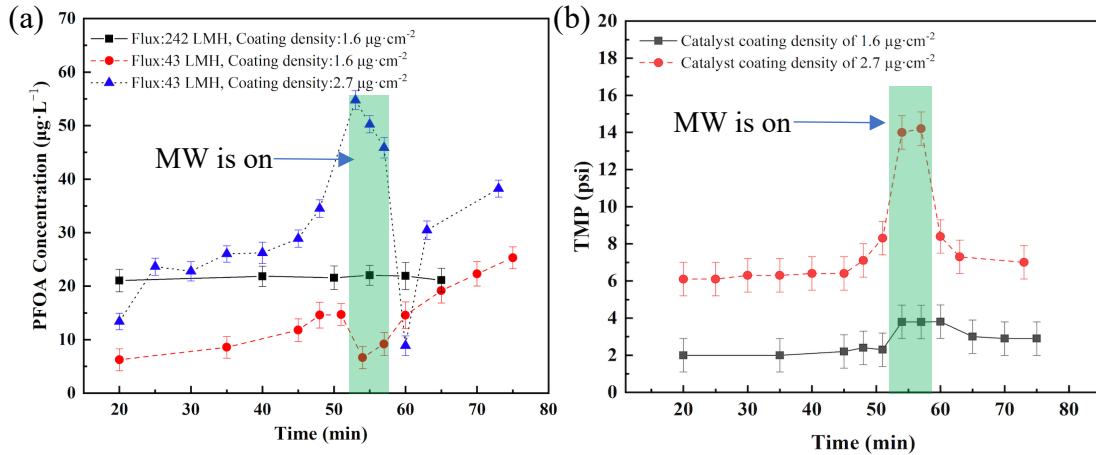
Figure 3.9 The changes of the permeate PFOA concentrations under different permeate flux and coating density (a) and TMP (b) with filtration time under a catalyst coating density of 1.6 µg·cm^{-2} and 2.7 µg·cm^{-2}. The initial spiked PFOA conentration: 25 µg·L^{-1} and microwave intensity: 125 watts.

3.4.4 Effect of Coated BFO Density

The PFOA concentrations in permeate water are compared in **Figure 3.9a** after the feed water passed through the two types of ceramic membranes with low and high BFO coating densities. The high coating density membrane appeared to achieve lower removal of PFOA than the low coating density membrane did. Li et al. indicated that excessive catalyst doses (above 1.0 g·L^{-1}) did not promote the degradation of PFOA under MW irradiation [88], because high doses of catalysts may interfere the microwave transmission or absorption. The electromagnetic wave attenuation can be observed inside the charge material during the microwave irradiation. As figure 3 showed, if a plane electromagnetic wave of a particular surface power density hits the microwave-adsorbing material (P_{in}), a part of its density is reflected (P_{out}), while another part is absorbed by the material. The microwave power density exponentially attenuates with the depth of the material surface

$$p_x = p_0 \cdot e^{-2x/D_p} \tag{3.2}$$

where p_x is the volume microwave power density in microwave-adsorbing material at a distance x (m) from the surface (watt·m^{-3}), p_0 is power per volume unit at surface (watt·m^{-3}), D_p is penetration depth (m). The penetration depth (D_p) of microwave at 2.45 GHz is generally in the order of a few centimeters, which highly depends on the dielectric permittivity (ε) of the microwave-absorbing materials [117-119]. It is worth noting that the relative dielectric permittivity also changes with the electrical parameters and the frequency of the electromagnetic wave. **Table 3.2** shows an exemplary value of relative electrical permittivity and field penetration depth at a frequency of 3 GHz for different materials. Thus, high density of catalyst may not favor the penetration of microwave for catalytic degradation reactions. Instead, the excessive BFO catalyst may adsorb and accumulate PFOA. As the two types of membranes were pre-conditioned to stabilize the filtration system by passing the same feed solution of PFOA for 20 min, the permeate PFOA concentration from the high-density coated membrane is observed to be higher than that of from the low-density coated membrane, which may result from the adsorption effect of excessive BFO catalyst and progressive release over time of filtration.

Figure 3.9b compares the monitored transmembrane pressure (TMP) that increased substantially after microwave irradiation (53 min-58 min). The TMP increase was less significant for the low coating density membrane (1.6 μg·cm^{-2}). The potential causes of substantial TMP increase are that water molecules may strongly absorb microwave energy and transform into micro/nanobubbles that may block the passage of permeate water. Moreover, the increase of the permeate water results in reduced solubility of dissolved gases (e.g., air) that also vaporize and interfere the filtration process [120].
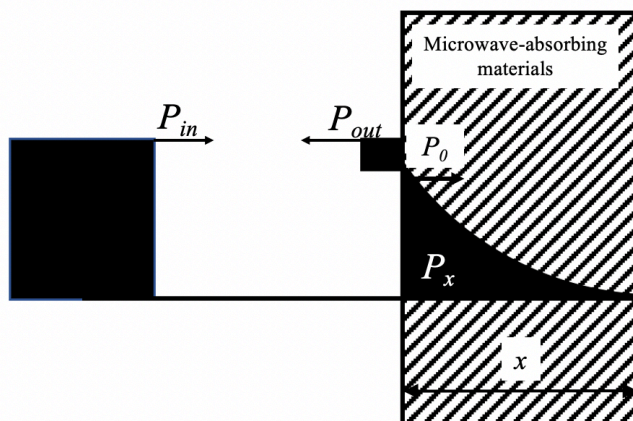
Figure 3.10 The distribution of power density absorbed by the microwave-absorbing materials at a plane wave.

Table 3.2 Electrical Permittivity of Materials and Penetration Depth

Material	T (°C)	ε	D_p (m)
Water	25	76.7	0.023
Ice	-12	3.20	19.77
Polystyrene	25	2.55	60.42
Teflon	25	2.10	146.44
Table salt	25	2.26	32.76
Aluminium oxide	25	8.79	3.62
Fused quartz	25	3.78	246.91

3.5 Major Intermediates and Degradation Mechanism

3.5.1 Detection of Fluoride Ions Using Ion Chromatography (IC)

The incomplete release of fluoride ion indicated that PFOA, although effectively decomposed via this microwave assisted photo-Fenton reaction, may be converted to other organic byproducts as reported elsewhere.[121, 122] For example, PFOA degradation may follow a stepwise CF_2 flake-off manner toward short-chain PFOAs under catalytic

degradation.[123]The generation of inorganic fluoride (F⁻) and formate ions concentration during the degradation reaction usually be used to prove the efficient degradation of PFOA. [124, 125] For instance, the main intermediates in PFOA degradation were formate and F⁻ ions which rapidly reached their maximum concentration after 60 min of photodegradation reaction, indicating the direct C-F bond cleavage in PFOA. [126] Therefore, to further confirm the degradation of PFOA, the fluoride ion in the solution was analyzed by an ion chromatography (IC). The inlet sample (0.5 ml) and outlet sample (0.4 ml) were collected for the IC detection. **Table 3.3** shows that fluoride ion concentrations of outlet (0.15 mg·L⁻¹) was higher than the concentration of inlet (0.08 mg·L⁻¹), proving the release of fluoride ion in the process of PFOA degradation. The defluorination (R, %) is 20% as defined by following equation: [1]

$$R(\%) = \frac{C_{F^-} \times 100}{15 \times C_{PFOA_0}} \tag{3.3}$$

where, C_{F^-} is the concentration of fluoride ions; C_{PFOA0} is the initial concentrations of PFOA (0.05 mg·L⁻¹). In the following experiments, we will collect more than 7 ml effluent to further prove the above result.

Table 3.3 The Fluoride Ion Concentration of Inlet and Outlet Samples Detected by IC

Type	Permeate flux (LHM)	Hydraulic retention time (min)	Concentration (mg·L⁻¹)
Inlet			0.08 ± 0.01
	43	6.71	
Outlet			0.15 ± 0.01

3.5.2 Detection of Major Intermediates by LC/QQQ Mass Spectrometry

Previous authors reported sequential degradation, losing one CF_2 unit at a time from PFOA and its intermediates step-by-step during PS oxidation, and yielding a mixture of shorter-chain-length compounds (i.e., PFHpA, PFHxA, PFPeA, and PFBA) as degradation intermediates.[127-129] A liquid chromatography (LC) coupled with triple-quadrupoles MS (QQQ) mass spectrometer in MRM mode with negative ESI was used to determine the concentrations of PFOA in the effluent and the major degradation products of PFOA. The full scan of outlet sample was performed, showed in **Figure 3.11a**. By comparing the mass and charge rate in PFAS and full scan spectrum, the spectrum at m/z 118.9, 169, 213,263 and 319 correspond to PFHxA (C6), PFOA (C8), PFBA (C4), PFPeA (C5) and PFHpA (C7), respectively, shown in Figure 3.2. [44, 130, 131] Therefore, we speculate that they may be the intermediates of PFOA degradation. Other characteristic peaks are probably caused by solvents or impurities from the PFOA sample. In addition, to further prove the finding, we use the eight PFAS standards (PFBS, PFHxA, PFHpA, PFHxS, PFOA, PFOS, PFPeA and PFNA), which calibration curves had been prepared in section 2.9.2, to quantify the concentration of intermediates. **Figure 3.11b** shows that the PFPeA have been detected in the outlet samples using established PFPeA calibration curves. The increased concentration of PFPeA under the microwave irradiation indicated that PFPeA may be the main intermediate of PFOA degradation.
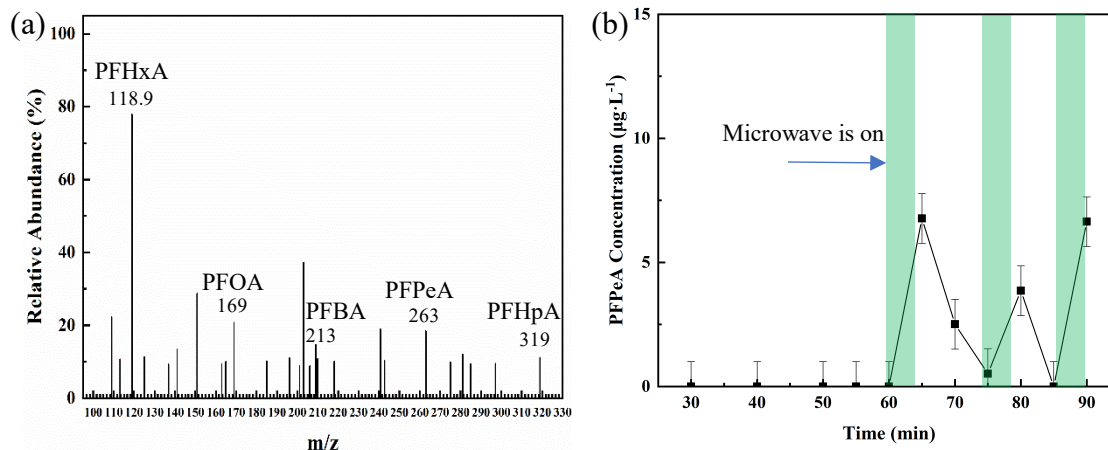
Figure 3.11 MS full scan spectrum of outlet PFOA sample (a) and the PFPeA concentration change with filtration time (b). The initial spiked PFOA conentration: 25 $\mu g \cdot L^{-1}$; microwave intensity: 125 watt; cataslyt coating density: 1.6 $\mu g \cdot cm^{-2}$, and permeate flux: 43 LMH.

3.5.3 Analysis of PFOA Degradation Mechanism

Figure 3.12 shows that PFOA exhibited stepwise decomposition via release of $-CF_2$ groups and transformation into short-chain PFAAs.[132] The concentrations of the PFAA intermediates increased with increasing reaction time in the photoelectrochemical (PEC) system, and the order of their concentrations was PFHpA (C7) >PFHxA (C6) >PFPeA (C5) > PFBA (C4) > PFPA (C3). Based on the shorter chain intermediate products of PFOA we detected before and other studies investigating PFOA decomposition, possible PFOA degradation pathways in the presence of ·OH under microwave irradiation are shown in **Eq. 3.4-3.6**. Longer carbon chains (e.g., $C_7F_{15}COOH$) broke up at first, followed by the fragmentation of the C-C bond between the C_7F_{15} and COO^- into $C_7F_{15}\cdot$ and CO_2. Among all of the $-CF_2-$ in a PFOA molecule, the α-position one adjacent to the carboxyl group has exhibited a high activity likely due to the inductive effect of the headgroup, thereby providing the preferential reaction center.[133] Next, the $C_7F_{15}\cdot$ radical is immediately hydrolyzed and converted into $C_6F_{13}COOH$ and F^- ion. The intermediate $C_6F_{13}COOH$ is further eliminated into a series of perfluorinated carboxylic acids as we

detected above.[88] In addition, PFASs showed an initial period of rapid F⁻ release, followed by slower F⁻ release before reaching a plateau, and the decay of CF₃−COO⁻ took 24 h to complete while the deF % was almost 100%, whereas the decay of all longer PFCAs took 8−12 h to complete, but the maximal deF % was ∼55%.[134]This indicate that the long chains of PFAS is easier to break than short chains.

$$C_7F_{15}COO^- + \cdot OH \rightarrow C_7F_{15}COO \cdot + HO^- \tag{3.4}$$

$$C_7F_{15}COO \cdot \rightarrow CO_2 + C_7F_{15} \cdot \tag{3.5}$$

$$C_7F_{15} \cdot + 2H_2O \rightarrow C_6F_{13}COOH + 2F^- + 2H^+ + H \tag{3.6}$$
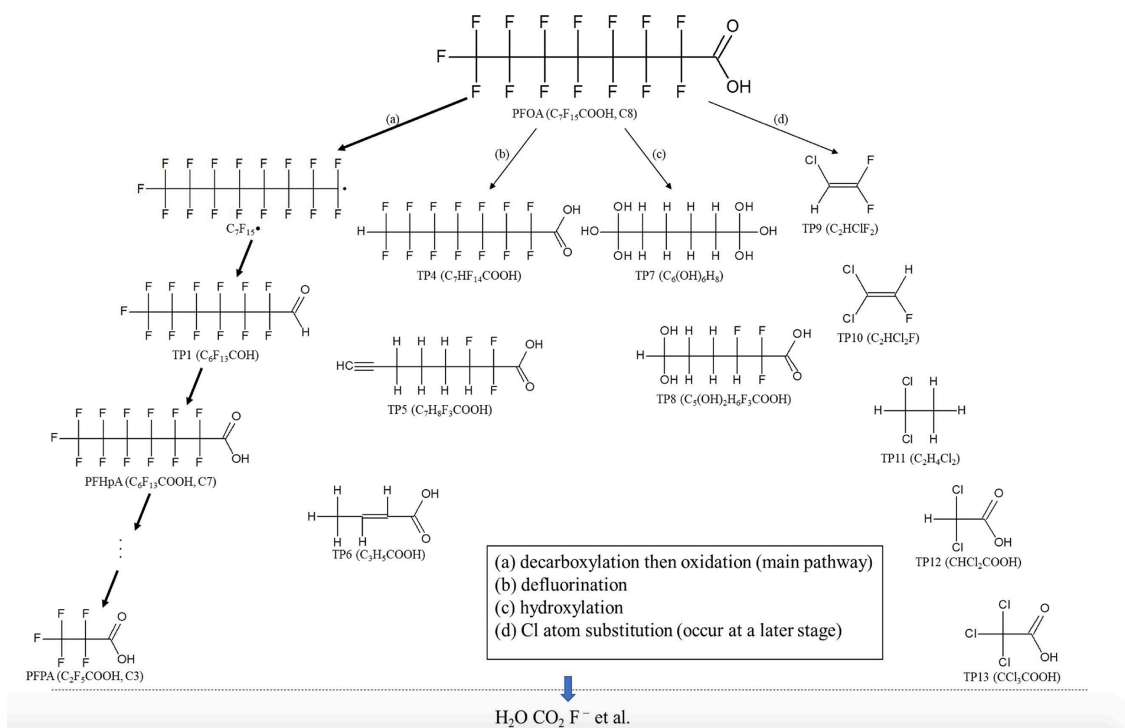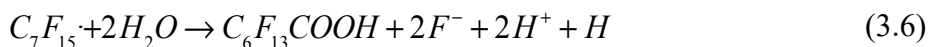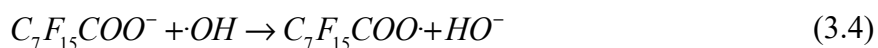
Figure 3.12 Possible PFOA degradation pathways

Source: [132]

3.6 Interference of PFOA to Total Organic Carbon Analyzer

Total Organic Carbon (TOC), as an important index of mineralization, have been widely used to evaluate the degradation degree of PFOA. TOC analyzers measure the CO_2 formed when organic carbon is oxidized and when inorganic carbon is acidified. In a combustion analyzer, half of the sample is injected into a chamber where it is acidified, usually with phosphoric acid, to turn all of the inorganic carbon into carbon dioxide as per the following reaction:

$$CO_2 + H_2O \leftrightarrow H_2CO_3 \leftrightarrow H^+ + HCO_3^- \leftrightarrow 2H^+ + CO_3^{2-} \tag{3.7}$$
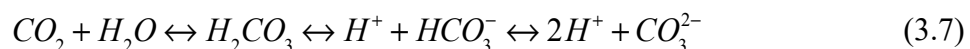
This is then sent to a detector for measurement. The other half of the sample is injected into a combustion chamber which is raised to between 600–700 °C, some even up to 1200 °C. Here, all the carbon reacts with oxygen, forming carbon dioxide. It's then flushed into a cooling chamber, and finally into the detector. By finding the total inorganic carbon and subtracting it from the total carbon content, the amount of organic carbon is determined. However, **Figure 3.13** showed that theoretical TOC value, calculated by **Eqution 3.8**, may be inconsistent with the measured TOC: When the theoretical value is less than 2.5ppb, it has a linear relationship with the measured value, While the measured value is significantly smaller than the measured value when theoretical value is greater than 2.5ppb. We speculate that TOC analyzer, which utilizes a catalytic oxidation combustion technique at high temperature to convert organic carbon into CO_2, would be hard to convert the organic carbon of PFOA to CO_2 completely. Therefore, the calibration curve is prepared to correlate the measured TOC with the theoretical TOC based on PFOA concentration.

$$TOC_{theoretical} = \frac{M_{Carbon}}{M_{PFOA}} \times C_{PFOA} \tag{3.8}$$

where, M_{carbon} is the total molar mass of carbon in PFOA (g/mol); M_{PFOA} is the molar mass

of PFOA (g/mol); C_{PFOA} is the concentration of PFOA (g/L). The TOC of PFOA

degradation in the microwave-Fenton will be detected in further research to analyze the

degree of mineralization. For instance, Beatriz et.al reported that TOC was reduced by 62%

during the photocatalytic decomposition of PFOA.[127] **Figure 3.14** presents the change of

measured TOC and calculated TOC with reaction time. The difference between the PFOA

degradation (93%) and TOC reduction is attributed to the production of intermediates. It is

reported that the concentrations of PFOA, PFHpA, PFHxA, and PFPeA have a good match

with TOC decrease. The results proved the step-by-step PFOA degradation pathway

contributed to the intermediate products which are shorter-chain perfluoro carboxylates.
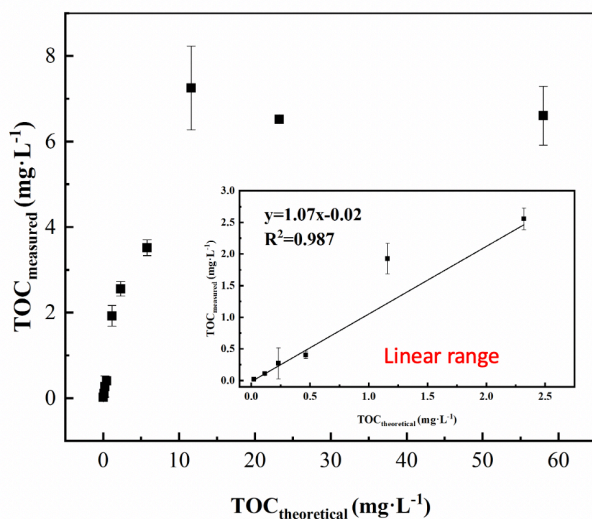
Figure 3.13 Calibration curves are prepared to correlate the measured TOC with the theoretical TOC based on different PFOA concentration (0.1 ppm, 0.5ppm, 1ppm, 2 ppm, 5ppm, 10 ppm, 25 ppm, 50 ppm, 100 ppm, 250 ppm).
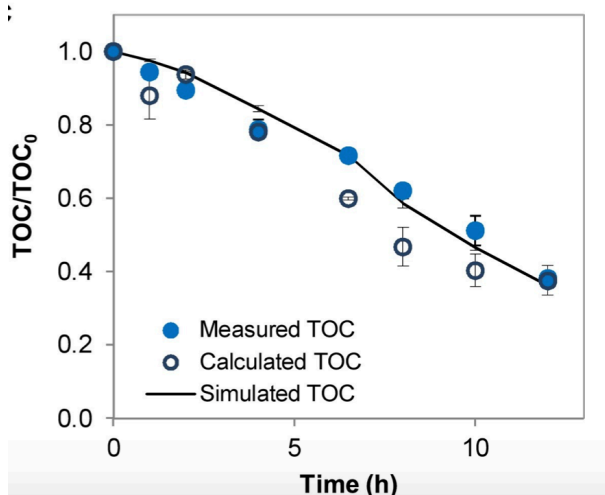
Figure 3.14 The change of measured TOC/TOC_0, calculated TOC/TOC_0 with reaction time.

Source:[127]

3.7 Detection of Quality Indicators and PFOA in Surface Raw Water

In order test the performance of PFOA degradation in actual water environment, we use microwave- enhanced membrane filtration system to treat PFOA which spiked in surface raw water. The surface raw water has been collected from Haworth in New Jersey. After 0.45-µm filtration of surface raw water sample, we tested water quality indicators of the raw water, showed in **Table 3.4**, and then spike a PFOA concentration of 50 $\mu g \cdot L^{-1}$ into the raw water to examine the matrix effect on the degradation efficiency under the same experimental condition as section 3.5.1. However, we found that the surface raw water sample which spiked 50 $\mu g \cdot L^{-1}$ PFOA was only detected by LC/QQQ at a concentration of 7 ± 2 $\mu g \cdot L^{-1}$. The reason is that numerous minerals, ions, particles, bacteria in surface raw water affect the response of LC/QQQ to PFOA. In addition, some researchers proved that the most widely used instrumentation for determining concentrations of PFAS in environmental samples is liquid chromatography–tandem mass spectrometry (LC–MS/MS) coupled with a solid-phase extraction (SPE) sample preparation step, showed in **Figure**

3.14 The popularity of this procedure is that diverse SPE sorbent chemistries have ability to bind a wide variety of molecules and ensure the selectivity and sensitivity of LC–MS/MS. [135, 136] Therefore, in order to analyze the performance of PFOA degradation in raw water, SPE sample preparation step followed by EPA 537 were introduced to avoid the influence of other substances in the water on the sensitivity of LC/QQQ.

Table 3.4 The Quality Indicator of Surface Raw Water

Quality indicators	pH	TP (mgPO$_4$/L)	TN (mgN/L)	TOC (mg/L)	ALK (mg/L as CaCO$_3$)	Conductivity (mmho/cm)	Nirite (mgN/L)	Ammonia (mgN/L)
Conc.	7.45±0.5	0.55±0.1	<0.5	4.26±0.1	78.75±5	450.5±50	<0.5	<0.5
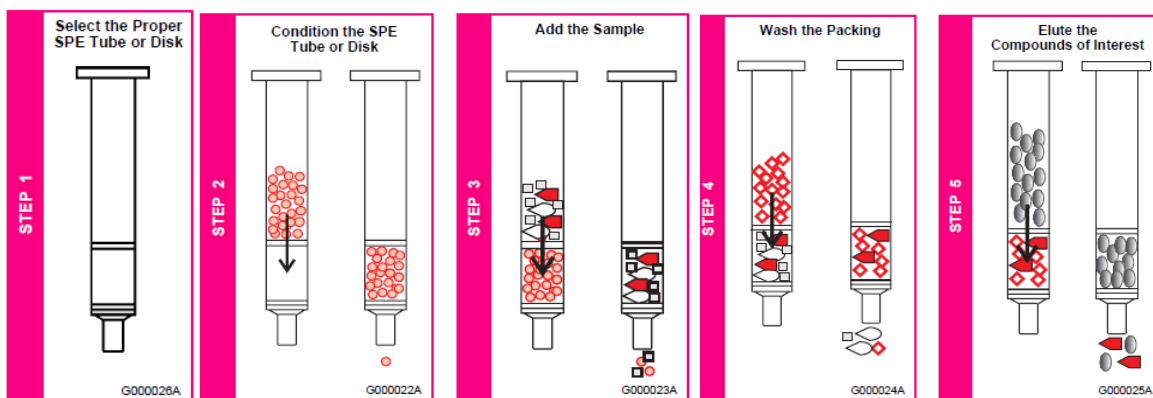
Figure 3.15 The schematic for SPE.

Source: [137]

3.8 Extraction Efficiency Assessment for Standard Samples

We employed the samples with DI water, spiked seven mixed PFAS at 10 ppt and 16ppt and LRB DI water respectively. All samples were extracted following the procedure as

mentioned previously. The recovery efficiency will be tested by 7 parallel tests based on following equation:

$$R = \frac{A}{B} \times 100\% \qquad (3.7)$$

where A is actual PFAS concentration after SPE procedure, B is theoretical PFAS concentration. **Table 3.5** shows that the recovering efficiencies of PFOS and PFOA reach 87% and 88%, respectively, while the PFHpA and PFHxA only have the recovery efficiencies of 14% and 10%, respectively, which may indicate the limited capability of SPE procedure to extract PFHpA and PFHxA. For low efficiency chemicals, improving the SPE procedure by adding soak time during conditioning the cartridge, making the transfer tube shorter, and using adapter on cartridge and smaller diameter during sample transfer.

Table 3.5 Recovering Efficiencies for Spiked Seven Mixed PFAS Samples

	Recovery efficiency (%)
PFOS	87±5
PFOA	88±3
PFNA	54±1
PFBS	72±1
PFHpA	14±2
PFHxS	40±1.5
PFHxA	10±1

3.9 Compare with Other AOPs

Many advanced oxidation processes (AOP) such as electrochemical technology, photo-Fenton, and photocatalytic technology have been developed for PFOA degradation as compared in **Table 3.6**. All these previous AOPs were conducted in the batch mode reaction with long reaction times and high PFOA concentrations at level of a few mg·L^{-1}. For instance, Saleem et al. introduced self-pulsing discharge (SPD) plasma reactor to decompose PFOA and reduced 84% of PFAS within 30 min [138]. Javed et al. applied continuous UV irradiation for 20 hours and removed 21% of PFOA [139]. Clearly, microwave-Fenton-like process in our study enables a continuous treatment with a shorter reaction time. Recently, combining AOPs with membrane filtration is increasingly recognized to enhance pollutant rejection or degradation. For example, Shi et al employed reactive electrochemical membrane and achieved 98.3% reduction of PFOS (1 mg·L^{-1}) at 4 mA·cm^{-2} (an anodic potential of 3.15 V) within 2 h [140]. Reactive membrane filtration is known to bring in benefits such as enhanced mass transfer across catalyst/liquid interface and increased reaction efficiencies toward refractory pollutants.

Table 3.6 Comparison of Treatment Performances of Different Treatment Techniques

Process	Initial concentration of PFAS (mg·L^{-1})	Reaction time	Removal rate (%)	Removal rate per miniute (mg·L^{-1}·min^{-1})	Removal rate per watt (mol·watt^{-1})	Ref.
Self-pulsing discharge (SPD) plasma reactor	41.4	0.5 h	84	1.15	3.5×10^{-9}	138
UV/TiO$_2$-rGO	0.58	8 h	86	10^{-3}	6.9×10^{-9}	141
UV/ BiOI$_{0.95}$Br$_{0.05}$	20	1.5 h	96	0.21	7.7×10^{-6}	142
Electrochemical Oxidation on BND	50	1.5 h	99.3	0.552	0.03	143

Reactive electrochemical membrane system	1	2 h	98.3	8.2×10^{-3}	4.6×10^{-7}	[140]
Microwave/BFO/H_2O_2	0.025	5 min	65.9	3.3×10^{-3}	2×10^{-9}	Present study

CONCLUSIONS

This study characterized membrane coating and examined the impacts of catalyst coating and microwave irradiation (or solution temperature increase) on membrane permeability. The root mean square (RMS) roughness, Rq, and Power Spectral Density (PSD) were determined by AFM for the three membrane samples based on surface morphology mapping. The water permeability of pristine and coated membrane indicated that membrane pore blocking by catalyst particles was not detrimental (reduced by 14%-22% compared to the pristine membrane). Meanwhile, the Carman-Kozeny model prediction well matched the experimental measurement of the permeability of feed solution under different temperatures, suggesting the enhanced permeation under microwave irradiation resulted from the water viscosity changes. High catalyst coating densities on membrane surface likely reduce permeability and adsorb PFOA, which will leach out without sufficient degradation. By contrast, moderate coating (1.6 μg·cm^{-2}) and low hydraulic retention time (2 min) enabled effective degradation of refractory PFOA through the presented microwave-assisted membrane filtration. The degradation by-product analysis indicated that the mineralization of PFOA was not complete as significant levels of PFPeA were detected. Furthermore, the interference of PFOA to TOC analyser was assessed, and a calibration curve is prepared to correlate the measured TOC with the theoretical TOC based on PFOA concentration. To make preparation for PFOA degradation in nature water, the quality indicator of surface raw water collected from Haworth in New Jersey was obtained, and SPE coupled LC/QQQ system was built followed by EPA 537. In sum, future studies are still needed to develop novel catalysts and rational operational strategies to

improve mineralization of PFOA and other PFAS within this reactive membrane filtration

process.

REFERENCES

1. Xing, D. Y.; Chen, Y.; Zhu, J.; Liu, T., Fabrication of hydrolytically stable magnetic core-shell aminosilane nanocomposite for the adsorption of PFOS and PFOA. *Chemosphere* **2020**, 126384.
2. Xu, J.; Liu, Z.; Zhao, D.; Gao, N.; Fu, X., Enhanced adsorption of perfluorooctanoic acid (PFOA) from water by granular activated carbon supported magnetite nanoparticles. *Science of The Total Environment* **2020**, 137757.
3. Lindstrom, A. B.; Strynar, M. J.; Libelo, E. L., Polyfluorinated compounds: past, present, and future. *Environmental Science & Technology* **2011**, *45*, 7954-7961.
4. Post, G. B.; Cohn, P. D.; Cooper, K. R., Perfluorooctanoic acid (PFOA), an emerging drinking water contaminant: a critical review of recent literature. *Environmental research* **2012**, *116*, 93-117.
5. Kunacheva, C.; Fujii, S.; Tanaka, S.; Seneviratne, S.; Lien, N. P. H.; Nozoe, M.; Kimura, K.; Shivakoti, B. R.; Harada, H., Worldwide surveys of perfluorooctane sulfonate (PFOS) and perfluorooctanoic acid (PFOA) in water environment in recent years. *Water Science and Technology* **2012**, *66*, 2764-2771.
6. Prevedouros, K.; Cousins, I. T.; Buck, R. C.; Korzeniowski, S. H., Sources, fate and transport of perfluorocarboxylates. *Environmental science & technology* **2006,** *40*, 32-44.
7. Giesy, J. P.; Kannan, K., Global distribution of perfluorooctane sulfonate in wildlife. *Environmental science & technology* **2001,** *35*, 1339-1342.
8. Clara, M.; Scharf, S.; Weiss, S.; Gans, O.; Scheffknecht, C., Emissions of perfluorinated alkylated substances (PFAS) from point sources—identification of relevant branches. *Water science and technology* **2008,** *58*, 59-66.
9. Olsen, G. W.; Mair, D. C.; Church, T. R.; Ellefson, M. E.; Reagen, W. K.; Boyd, T. M.; Herron, R. M.; Medhdizadehkashi, Z.; Nobiletti, J. B.; Rios, J. A., Decline in perfluorooctanesulfonate and other polyfluoroalkyl chemicals in American Red Cross adult blood donors, 2000− 2006. *Environmental science & technology* **2008,** *42*, 4989-4995.
10. des Umweltbundesamtes, B., Referenzwerte für Perfluoroctansäure (PFOA) und Perfluoroctansulfonsäure (PFOS) im Blutplasma. **2009**.
11. Dickenson, E. R.; Higgins, C., Treatment Mitigation Strategies for Poly-and Perfluoroalkyl Substances [Project# 4322]. **2016**.
12. Suja, F.; Pramanik, B. K.; Zain, S. M., Contamination, bioaccumulation and toxic effects of perfluorinated chemicals (PFCs) in the water environment: a review paper. *Water Science and Technology* **2009,** *60*, 1533-1544.
13. Fei, C.; McLaughlin, J. K.; Lipworth, L.; Olsen, J., Maternal levels of perfluorinated chemicals and subfecundity. *Human Reproduction* **2009,** *24*, 1200-1205.
14. Lau, C.; Butenhoff, J. L.; Rogers, J. M., The developmental toxicity of perfluoroalkyl acids and their derivatives. *Toxicology and applied pharmacology* **2004,** *198*, 231-241.
15. Lau, C.; Thibodeaux, J. R.; Hanson, R. G.; Narotsky, M. G.; Rogers, J. M.; Lindstrom, A. B.; Strynar, M. J., Effects of perfluorooctanoic acid exposure during pregnancy in the mouse. *Toxicological Sciences* **2006,** *90*, 510-518.

16. Butenhoff, J. L.; Kennedy Jr, G. L.; Frame, S. R.; O'Connor, J. C.; York, R. G., The reproductive toxicology of ammonium perfluorooctanoate (APFO) in the rat. *Toxicology* **2004,** *196*, 95-116.

17. Case, M. T.; York, R. G.; Christian, M. S., Rat and rabbit oral developmental toxicology studies with two perfluorinated compounds. *International journal of toxicology* **2001,** *20*, 101-109.

18. Kawashima, Y.; Kobayashi, H.; Miura, H.; Kozuka, H., Characterization of hepatic responses of rat to administration of perfluorooctanoic and perfluorodecanoic acids at low levels. *Toxicology* **1995,** *99*, 169-178.

19. Kudo, N.; Iwase, Y.; Okayachi, H.; Yamakawa, Y.; Kawashima, Y., Induction of hepatic peroxisome proliferation by 8–2 telomer alcohol feeding in mice: formation of perfluorooctanoic acid in the liver. *Toxicological sciences* **2005,** *86*, 231-238.

20. DiGangi, J.; Blum, A.; Bergman, Å.; de Wit, C. A.; Lucas, D.; Mortimer, D.; Schecter, A.; Scheringer, M.; Shaw, S. D.; Webster, T. F., San Antonio statement on brominated and chlorinated flame retardants. *Environmental health perspectives* **2010,** *118*, A516-A518.

21. Blum, A.; Balan, S. A.; Scheringer, M.; Trier, X.; Goldenman, G.; Cousins, I. T.; Diamond, M.; Fletcher, T.; Higgins, C.; Lindeman, A. E., The Madrid statement on poly-and perfluoroalkyl substances (PFASs). *Environmental health perspectives* **2015,** *123*, A107-A111.

22. FACT SHEET PFOA & PFOS Drinking Water Health Advisories. *U.S. Environmental Protection Agency (USEPA)* **2016**.

23. Hu, X. C.; Andrews, D. Q.; Lindstrom, A. B.; Bruton, T. A.; Schaider, L. A.; Grandjean, P.; Lohmann, R.; Carignan, C. C.; Blum, A.; Balan, S. A., Detection of poly-and perfluoroalkyl substances (PFASs) in US drinking water linked to industrial sites, military fire training areas, and wastewater treatment plants. *Environmental science & technology letters* **2016,** *3*, 344.

24. Schaefer, C. E.; Andaya, C.; Burant, A.; Condee, C. W.; Urtiaga, A.; Strathmann, T. J.; Higgins, C. P., Electrochemical treatment of perfluorooctanoic acid and perfluorooctane sulfonate: Insights into mechanisms and application to groundwater treatment. *Chemical Engineering Journal* **2017,** *317*, 424-432.

25. Choi, G.-H.; Lee, D.-Y.; Jeong, D.-K.; Kuppusamy, S.; Lee, Y. B.; Park, B.-J.; Kim, J.-H., Perfluorooctanoic acid (PFOA) and perfluorooctanesulfonic acid (PFOS) concentrations in the South Korean agricultural environment: a national survey. **2017**.

26. Boonya-Atichart, A.; Boontanon, S. K.; Boontanon, N., Removal of perfluorooctanoic acid (PFOA) in groundwater by nanofiltration membrane. *Water Science and Technology* **2016,** *74*, 2627-2633.

27. Boonya-atichart, A.; Boontanon, S. K.; Boontanon, N., Study of hybrid membrane filtration and photocatalysis for removal of perfluorooctanoic acid (PFOA) in groundwater. *Water Science and Technology* **2018,** *2017*, 561-569.

28. Espana, V. A. A.; Mallavarapu, M.; Naidu, R., Treatment technologies for aqueous perfluorooctanesulfonate (PFOS) and perfluorooctanoate (PFOA): A critical review with an emphasis on field testing. *Environmental Technology & Innovation* **2015,** *4*, 168-181.

29. Bao, Y.; Cagnetta, G.; Huang, J.; Yu, G., Degradation of hexafluoropropylene oxide oligomer acids as PFOA alternatives in simulated nanofiltration concentrate: Effect of molecular structure. *Chemical Engineering Journal* **2020,** *382*, 122866.

30. Gu, Y.; Dong, W.; Wang, H., Degradation of Perfluorooctane Sulfonate (PFOS) by Nanofiltration Membrane Enrichment-VUV/Sulfite Reduction. *DEStech Transactions on Environment, Energy and Earth Sciences* **2017**.

31. Baudequin, C.; Mai, Z.; Rakib, M.; Deguerry, I.; Severac, R.; Pabon, M.; Couallier, E., Removal of fluorinated surfactants by reverse osmosis–role of surfactants in membrane fouling. *Journal of membrane science* **2014,** *458*, 111-119.

32. Dai, X.; Xie, Z.; Dorian, B.; Gray, S.; Zhang, J., Comparative study of PFAS treatment by UV, UV/ozone, and fractionations with air and ozonated air. *Environmental Science: Water Research & Technology* **2019,** *5*, 1897-1907.

33. Wang, T.; Zhao, C.; Li, P.; Li, Y.; Wang, J., Fabrication of novel poly (m-phenylene isophthalamide) hollow fiber nanofiltration membrane for effective removal of trace amount perfluorooctane sulfonate from water. *Journal of membrane science* **2015,** *477*, 74-85.

34. Rattanaoudom, R. Membrane hybrid system for removal of PFOS and PFOA in industrial waste water: Application of conventional adsorbents and nanoparticles. PhD dissertation Environmental Engineering and Management Inter-University …, 2011.

35. Zhou, Y.; He, Z.; Tao, Y.; Xiao, Y.; Zhou, T.; Jing, T.; Zhou, Y.; Mei, S., Preparation of a functional silica membrane coated on Fe3O4 nanoparticle for rapid and selective removal of perfluorinated compounds from surface water sample. *Chemical Engineering Journal* **2016,** *303*, 156-166.

36. Wang, Y.; Zhang, P., Photocatalytic decomposition of perfluorooctanoic acid (PFOA) by TiO2 in the presence of oxalic acid. *Journal of hazardous materials* **2011,** *192*, 1869-1875.

37. Dillert, R.; Bahnemann, D.; Hidaka, H., Light-induced degradation of perfluorocarboxylic acids in the presence of titanium dioxide. *Chemosphere* **2007,** *67*, 785-792.

38. Shao, T.; Zhang, P.; Jin, L.; Li, Z., Photocatalytic decomposition of perfluorooctanoic acid in pure water and sewage water by nanostructured gallium oxide. *Applied Catalysis B: Environmental* **2013,** *142*, 654-661.

39. Li, Z.; Zhang, P.; Shao, T.; Wang, J.; Jin, L.; Li, X., Different nanostructured In2O3 for photocatalytic decomposition of perfluorooctanoic acid (PFOA). *Journal of hazardous materials* **2013,** *260*, 40-46.

40. Song, Z.; Tang, H.; Wang, N.; Zhu, L., Reductive defluorination of perfluorooctanoic acid by hydrated electrons in a sulfite-mediated UV photochemical system. *Journal of hazardous materials* **2013,** *262*, 332-338.

41. Huang, J.; Wang, X.; Pan, Z.; Li, X.; Ling, Y.; Li, L., Efficient degradation of perfluorooctanoic acid (PFOA) by photocatalytic ozonation. *Chemical Engineering Journal* **2016,** *296*, 329-334.

42. Zsilák, Z.; Szabó-Bárdos, E.; Fónagy, O.; Horváth, O.; Horváth, K.; Hajós, P., Degradation of benzenesulfonate by heterogeneous photocatalysis combined with ozonation. *Catalysis today* **2014,** *230*, 55-60.

43. Ochiai, T.; Iizuka, Y.; Nakata, K.; Murakami, T.; Tryk, D. A.; Fujishima, A.; Koide, Y.; Morito, Y., Efficient electrochemical decomposition of perfluorocarboxylic acids by the use of a boron-doped diamond electrode. *Diamond and Related Materials* **2011,** *20*, 64-67.
44. Zhuo, Q.; Deng, S.; Yang, B.; Huang, J.; Yu, G., Efficient electrochemical oxidation of perfluorooctanoate using a Ti/SnO2-Sb-Bi anode. *Environmental science & technology* **2011,** *45*, 2973-2979.
45. Lin, H.; Niu, J.; Ding, S.; Zhang, L., Electrochemical degradation of perfluorooctanoic acid (PFOA) by Ti/SnO2–Sb, Ti/SnO2–Sb/PbO2 and Ti/SnO2–Sb/MnO2 anodes. *Water research* **2012,** *46*, 2281-2289.
46. Sathya, U.; Nithya, M.; Balasubramanian, N., Evaluation of advanced oxidation processes (AOPs) integrated membrane bioreactor (MBR) for the real textile wastewater treatment. *Journal of environmental management* **2019,** *246*, 768-775.
47. Wu, H.; Xu, X.; Shi, L.; Yin, Y.; Zhang, L.-C.; Wu, Z.; Duan, X.; Wang, S.; Sun, H., Manganese oxide integrated catalytic ceramic membrane for degradation of organic pollutants using sulfate radicals. *Water Research* **2019,** *167*, 115110.
48. Wang, S.; Tian, J.; Wang, Q.; Xiao, F.; Gao, S.; Shi, W.; Cui, F., Development of CuO coated ceramic hollow fiber membrane for peroxymonosulfate activation: a highly efficient singlet oxygen-dominated oxidation process for bisphenol a degradation. *Applied Catalysis B: Environmental* **2019,** *256*, 117783.
49. Qing, W.; Li, X.; Shao, S.; Shi, X.; Wang, J.; Feng, Y.; Zhang, W.; Zhang, W., Polymeric catalytically active membranes for reaction-separation coupling: A review. *Journal of Membrane Science* **2019**.
50. Chávez, A.; Gimeno, O.; Rey, A.; Pliego, G.; Oropesa, A.; Álvarez, P.; Beltrán, F., Treatment of highly polluted industrial wastewater by means of sequential aerobic biological oxidation-ozone based AOPs. *Chemical Engineering Journal* **2019,** *361*, 89-98.
51. Lin, H.; Niu, J.; Liang, S.; Wang, C.; Wang, Y.; Jin, F.; Luo, Q.; Huang, Q., Development of macroporous Magneli phase Ti4O7 ceramic materials: As an efficient anode for mineralization of poly-and perfluoroalkyl substances. *Chemical Engineering Journal* **2018,** *354*, 1058-1067.
52. Le, T. X. H.; Haflich, H.; Shah, A. D.; Chaplin, B. P., Energy-Efficient Electrochemical Oxidation of Perfluoroalkyl Substances Using a Ti4O7 Reactive Electrochemical Membrane Anode. *Environmental Science & Technology Letters* **2019,** *6*, 504-510.
53. Ganiyu, S. O.; Van Hullebusch, E. D.; Cretin, M.; Esposito, G.; Oturan, M. A., Coupling of membrane filtration and advanced oxidation processes for removal of pharmaceutical residues: a critical review. *Separation and Purification Technology* **2015,** *156*, 891-914.
54. Yuan, C.; Huang, Y.; Cannon, F. S.; Geng, C.; Liang, Z.; Zhao, Z., Removing PFOA and nitrate by quaternary ammonium compounds modified carbon and its mechanisms analysis: Effect of base, acid or oxidant pretreatment. *Chemosphere* **2020,** *242*, 125233.
55. Song, L.; Zhu, B.; Gray, S.; Duke, M.; Muthukumaran, S., Performance of Hybrid Photocatalytic-Ceramic Membrane System for the Treatment of Secondary Effluent. *Membranes* **2017,** *7*, 20.

56. Lim, T.-T.; Goei, R., Combined Photocatalysis–Separation Processes for Water Treatment Using Hybrid Photocatalytic Membrane Reactors. In *Photocatalysis*, 2016; pp 130-156.

57. Li, Q.; Jia, R.; Shao, J.; He, Y., Photocatalytic degradation of amoxicillin via TiO2 nanoparticle coupling with a novel submerged porous ceramic membrane reactor. *Journal of cleaner production* **2019,** *209*, 755-761.

58. Ahmad, R.; Kim, J. K.; Kim, J. H.; Kim, J., Diethylene glycol-assisted organized TiO2 nanostructures for photocatalytic wastewater treatment ceramic membranes. *Water* **2019,** *11*, 750.

59. Grant, E.; Halstead, B. J., Dielectric parameters relevant to microwave dielectric heating. *Chem. Soc. Rev.* **1998,** *27*, 213-224.

60. Yang, L.; Chen, Z.; Yang, J.; Liu, Y.; Wang, J.; Yu, Y.; Gao, X., Removal of volatile fatty acid in landfill leachate by the microwave-hydrothermal method. *Desalination and Water Treatment* **2014,** *52*, 4423-4429.

61. Ku, H. S.; Siores, E.; Taube, A.; Ball, J. A. R., Productivity improvement through the use of industrial microwave technologies. *Computers & Industrial Engineering* **2002,** *42*, 281-290.

62. Wang, Y.; Zhang, P., Photocatalytic decomposition of perfluorooctanoic acid (PFOA) by TiO_2 in the presence of oxalic acid. *J Hazard Mater* **2011,** *192*, 1869-75.

63. Qiu, Y.; Zhou, J.; Cai, J.; Xu, W.; You, Z.; Yin, C., Highly efficient microwave catalytic oxidation degradation of p-nitrophenol over microwave catalyst of pristine α-Bi 2 O 3. *Chem. Eng. J.* **2016,** *306*, 667-675.

64. Chen, J.; Pan, H.; Hou, H.; Li, H.; Yang, J.; Wang, L., High efficient catalytic degradation of PNP over Cu-bearing catalysts with microwave irradiation. *Chem. Eng. J.* **2017,** *323*, 444-454.

65. Lv, G.; Xing, X.; Liao, L.; An, P.; Yin, H.; Mei, L.; Li, Z., Synthesis of birnessite with adjustable electron spin magnetic moments for the degradation of tetracycline under microwave induction. *Chem. Eng. J.* **2017**.

66. Chen, J.; Xue, S.; Song, Y.; Shen, M.; Zhang, Z.; Yuan, T.; Tian, F.; Dionysiou, D. D., Microwave-induced carbon nanotubes catalytic degradation of organic pollutants in aqueous solution. *J. Hazard. Mater.* **2016,** *310*, 226-234.

67. Zhang, Z.; Jiatieli, J.; Liu, D.; Yu, F.; Xue, S.; Gao, W.; Li, Y.; Dionysiou, D. D., Microwave induced degradation of parathion in the presence of supported anatase- and rutile-TiO2/AC and comparison of their catalytic activity. *Chem. Eng. J.* **2013,** *231*, 84-93.

68. Stiegman, A., Loss Mechanisms and Microwave-Specific Effects in Heterogeneous Catalysis. *Microwaves in Catalysis: Methodology and Applications* **2015**.

69. Huang, N.; Xu, Y.; Jiang, D., High-performance heterogeneous catalysis with surface-exposed stable metal nanoparticles. *Scientific reports* **2014,** *4*, 7228.

70. Restrepo, J.; Porcar, R.; Lozano, P.; Burguete, M. I.; García-Verdugo, E.; Luis, S. V., Microwave-assisted selective oxidation of 1-phenyl ethanol in water catalyzed by metal nanoparticles immobilized onto supported ionic liquidlike phases. *ACS Catalysis* **2015,** *5*, 4743-4750.

71. Priya, S. S.; Selvakannan, P.; Chary, K. V.; Kantam, M. L.; Bhargava, S. K., Solvent-free microwave-assisted synthesis of solketal from glycerol using transition metal ions promoted mordenite solid acid catalysts. *Molecular Catalysis* **2017,** *434*, 184-193.

72. Kokel, A.; Schäfer, C.; Török, B., Application of microwave-assisted heterogeneous catalysis in sustainable synthesis design. *Green Chemistry* **2017,** *19*, 3729-3751.

73. Horikoshi, S.; Serpone, N., Role of microwaves in heterogeneous catalytic systems. *Catalysis Science & Technology* **2014,** *4*, 1197-1210.

74. Hu, E.; Cheng, H., Catalytic effect of transition metals on microwave-induced degradation of atrazine in mineral micropores. *Water Res.* **2014,** *57*, 8-19.

75. He, P.; Haswell, S. J.; Fletcher, P. D. I., Microwave heating of heterogeneously catalysed Suzuki reactions in a micro reactor. *Lab on a Chip* **2004,** *4*, 38-41.

76. Benaskar, F.; Patil, N. G.; Engels, V.; Rebrov, E. V.; Meuldijk, J.; Hulshof, L. A.; Hessel, V.; Wheatley, A. E. H.; Schouten, J. C., Microwave-assisted Cu-catalyzed Ullmann ether synthesis in a continuous-flow milli-plant. *Chem. Eng. J.* **2012,** *207-208*, 426-439.

77. Benaskar, F.; Patil, N. G.; Rebrov, E. V.; Ben‐Abdelmoumen, A.; Meuldijk, J.; Hulshof, L. A.; Hessel, V.; Schouten, J. C., Micro/Milliflow Processing with Selective Catalyst Microwave Heating in the Cu‐Catalyzed Ullmann Etherification Reaction: A μ2‐Process. *ChemSusChem* **2013,** *6*, 353-366.

78. Peng, Z.; Hwang, J.-Y.; Mouris, J.; Hutcheon, R.; Huang, X., Microwave penetration depth in materials with non-zero magnetic susceptibility. *ISIJ international* **2010,** *50*, 1590-1596.

79. Xu, W.; Chen, J.; Qiu, Y.; Peng, W.; Shi, N.; Zhou, J., Highly efficient microwave catalytic oxidation degradation of 4-nitrophenol over magnetically separable NiCo2O4-Bi2O2CO3 composite without adding oxidant. *Separation and Purification Technology* **2019,** *213*, 426-436.

80. Li, S.; Zhang, G.; Wang, P.; Zheng, H.; Zheng, Y., Microwave-enhanced Mn-Fenton process for the removal of BPA in water. *Chemical Engineering Journal* **2016,** *294*, 371-379.

81. Zhang, A.; Gu, Z.; Chen, W.; Li, Q.; Jiang, G., Removal of refractory organic pollutants in reverse-osmosis concentrated leachate by Microwave–Fenton process. *Environmental Science and Pollution Research* **2018,** *25*, 28907-28916.

82. Zhang, B.; You, H.; Wang, F., Microwave-enhanced catalytic wet peroxide oxidation of quinoline: the influence of pH and H 2 O 2 dosage and identification of reactive oxygen species. *RSC Advances* **2017,** *7*, 14769-14775.

83. Wang, N.; Wang, P., Study and application status of microwave in organic wastewater treatment – A review. *Chem. Eng. J.* **2016,** *283*, 193-214.

84. Hong, J.; Yuan, N.; Wang, Y.; Qi, S., Efficient degradation of Rhodamine B in microwave-H_2O_2 system at alkaline pH. *Chem. Eng. J.* **2012,** *191*, 364-368.

85. Zhao, G.; Gao, J.; Shi, W.; Liu, M.; Li, D., Electrochemical incineration of high concentration azo dye wastewater on the in situ activated platinum electrode with sustained microwave radiation. *Chemosphere* **2009,** *77*, 188-193.

86. Luo, W.; Zhu, L.; Wang, N.; Tang, H.; Cao, M.; She, Y., Efficient removal of organic pollutants with magnetic Nanoscaled BiFeO(3) as a reusable heterogeneous fenton-like catalyst. *Environ. Sci. Technol.* **2010,** *44*, 1786-91.

87. Li, S.; Zhang, G.; Zheng, H.; Wang, N.; Zheng, Y.; Wang, P., Microwave-assisted synthesis of BiFeO3nanoparticles with high catalytic performance in microwave-enhanced Fenton-like process. *RSC Adv.* **2016,** *6*, 82439-82446.

88. Li, S.; Zhang, G.; Zhang, W.; Zheng, H.; Zhu, W.; Sun, N.; Zheng, Y.; Wang, P., Microwave enhanced Fenton-like process for degradation of perfluorooctanoic acid (PFOA) using Pb-BiFeO3/rGO as heterogeneous catalyst. *Chemical Engineering Journal* **2017,** *326*, 756-764.

89. Fu, W.; Zhang, W., Microwave-enhanced membrane filtration for water treatment. *Journal of Membrane Science* **2018,** *568*, 97-104.

90. Einaga, H.; Nasu, Y.; Oda, M.; Saito, H., Catalytic performances of perovskite oxides for CO oxidation under microwave irradiation. *Chem. Eng. J.* **2016,** *283*, 97-104.

91. Sheng Deng, G. z., Shuwei Chen, Yanei Xue, Zhaolin Du and Peng Wang Rapid and effective preparation of a HPEI modified biosorbent based on cellulose fiber with a microwave irradiation method for enhanced arsenic removal in water. *J. Mater. Chem. A,* **2016,** *4*, 15851-15860.

92. Li, S.; Zhang, G.; Zheng, H.; Wang, N.; Zheng, Y.; Wang, P., Microwave-assisted synthesis of BiFeO 3 nanoparticles with high catalytic performance in microwave-enhanced Fenton-like process. *RSC Advances* **2016,** *6*, 82439-82446.

93. Alventosa-deLara, E.; Barredo-Damas, S.; Alcaina-Miranda, M. I.; Iborra-Clar, M. I., Study and optimization of the ultrasound-enhanced cleaning of an ultrafiltration ceramic membrane through a combined experimental–statistical approach. *Ultrasonics Sonochemistry* **2014,** *21*, 1222-1234.

94. Tripathi, B. P.; Dubey, N. C.; Choudhury, S.; Stamm, M., Antifouling and tunable amino functionalized porous membranes for filtration applications. *J. Mater. Chem.* **2012,** *22*, 19981-19992.

95. Vatanpour, V.; Madaeni, S. S.; Rajabi, L.; Zinadini, S.; Derakhshan, A. A., Boehmite nanoparticles as a new nanofiller for preparation of antifouling mixed matrix membranes. *Journal of membrane science* **2012,** *401*, 132-143.

96. Bear, J., Dynamics of fluids in porous media. Dover, New York. *Dynamics of fluids in porous media. Dover, New York.* **1972**, -.

97. Middleman, S., *An Introduction to Fluid Dynamics: Principles of Analysis and Design.* John Wiley & Sons Incorporated: 1998.

98. Carman, P., Fundamental principles of industrial filtration (A critical review of present knowledge). *Trans. Inst. Chem. Eng.* **1938,** *16*, 168-188.

99. Li, W.; Xing, W.; Xu, N., Modeling of relationship between water permeability and microstructure parameters of ceramic membranes. *Desalination* **2006,** *192*, 340-345.

100. Zheng, X.; Gao, W.; Zhang, X.; He, M.; Lin, X.; Cao, H.; Zhang, Y.; Sun, Z., Spent lithium-ion battery recycling – Reductive ammonia leaching of metals from cathode scrap by sodium sulphite. *Waste Management* **2017,** *60*, 680-688.

101. Tong, T.; Chen, J.; Jin, D.; Cheng, J., Preparation and gas sensing characteristics of BiFeO 3 crystallites. *Mater. Lett.* **2017,** *197*, 160-162.

102. Duparré, A.; Ferre-Borrull, J.; Gliech, S.; Notni, G.; Steinert, J.; Bennett, J. M., Surface characterization techniques for determining the root-mean-square roughness and power spectral densities of optical components. *Applied optics* **2002,** *41*, 154-171.

103. Shanmugharaj, A.; Ray, S.; Bandyopadhyay, S.; Bhowmick, A. K., Surface morphology of styrene-butadiene rubber vulcanizate filled with novel electron beam modified dual phase filler by atomic force microscopy. *Journal of adhesion science and technology* **2003,** *17*, 1167-1186.

104. Gómez-Rodríguez, J.; Asenjo, A.; Salvarezza, R.; Baró, A., Measuring the fractal dimension with STM: application to vacuum-evaporated gold. *Ultramicroscopy* **1992,** *42*, 1321-1328.

105. Sun, S.; Yao, H.; Fu, W.; Hua, L.; Zhang, G.; Zhang, W., Reactive Photo-Fenton ceramic membranes: Synthesis, characterization and antifouling performance. *Water research* **2018,** *144*, 690-698.

106. Carman, P. C., Fluid flow through granular beds. *Chemical Engineering Research and Design* **1997**, S32-S48.

107. Guo, H.; Zhao, S.; Wu, X.; Qi, H., Fabrication and characterization of TiO_2/ZrO_2 ceramic membranes for nanofiltration. *Microporous and Mesoporous Materials* **2018,** *260*, 125-131.

108. Xiangli, F.; Chen, Y.; Jin, W.; Xu, N., Polydimethylsiloxane (PDMS)/Ceramic Composite Membrane with High Flux for Pervaporation of Ethanol−Water Mixtures. *Industrial & Engineering Chemistry Research* **2007,** *46*, 2224-2230.

109. Chae, S.-R.; Yamamura, H.; Ikeda, K.; Watanabe, Y., Comparison of fouling characteristics of two different poly-vinylidene fluoride microfiltration membranes in a pilot-scale drinking water treatment system using pre-coagulation/sedimentation, sand filtration, and chlorination. *Water Res.* **2008,** *42*, 2029-2042.

110. Suzuki, T.; Watanabe, Y.; Ozawa, G.; Ikeda, S., Removal of soluble organics and manganese by a hybrid MF hollow fiber membrane system. *Desalination* **1998,** *117*, 119-129.

111. Tseng, W. J.; Lin, R.-D., BiFeO3/α-Fe2O3 core/shell composite particles for fast and selective removal of methyl orange dye in water. *Journal of colloid and interface science* **2014,** *428*, 95-100.

112. Luo, L.; Shen, K.; Xu, Q.; Zhou, Q.; Wei, W.; Gondal, M., Preparation of multiferroic Co substituted BiFeO3 with enhanced coercive force and its application in sorption removal of dye molecules from aqueous solution. *Journal of Alloys and Compounds* **2013,** *558*, 73-76.

113. Zhang, J.; Gondal, M.; Wei, W.; Zhang, T.; Xu, Q.; Shen, K., Preparation of room temperature ferromagnetic BiFeO3 and its application as an highly efficient magnetic separable adsorbent for removal of Rhodamine B from aqueous solution. *Journal of Alloys and Compounds* **2012,** *530*, 107-110.

114. Shang, E.; Li, Y.; Niu, J.; Li, S.; Zhang, G.; Wang, X., Photocatalytic degradation of perfluorooctanoic acid over Pb-BiFeO3/rGO catalyst: Kinetics and mechanism. *Chemosphere* **2018,** *211*, 34-43.

115. Petala, A.; Spyrou, D.; Frontistis, Z.; Mantzavinos, D.; Kondarides, D. I., Immobilized Ag3PO4 photocatalyst for micro-pollutants removal in a continuous flow annular photoreactor. *Catalysis Today* **2019,** *328*, 223-229.

116. Damodar, R. A.; Swaminathan, T., Performance evaluation of a continuous flow immobilized rotating tube photocatalytic reactor (IRTPR) immobilized with TiO2 catalyst for azo dye degradation. *Chemical Engineering Journal* **2008,** *144*, 59-66.

117. Schmink, J. R.; Leadbeater, N. E., Microwave heating as a tool for sustainable chemistry. *Microwave heating as a tool for sustainable chemistry. CRC Press, Boca Raton, FL* **2010**, 1-24.

118. Kappe, C. O., Controlled Microwave Heating in Modern Organic Synthesis. *Angew. Chem. Int. Ed.* **2004,** *43*, 6250-6284.

119. de la Hoz, A., Microwave Heating as a Tool for Sustainable Chemistry. Edited by Nicholas E. Leadbeater. Wiley Online Library: 2011.

120. Elperin, T.; Fominykh, A.; Krasovitov, B., Evaporation and condensation of large droplets in the presence of inert admixtures containing soluble gas. *Journal of the Atmospheric Sciences* **2007,** *64*, 983-995.

121. Liu, S.-T.; Zhang, A.-B.; Yan, K.-K.; Ye, Y.; Chen, X.-G., Microwave-enhanced catalytic degradation of methylene blue by porous MFe2O4 (M= Mn, Co) nanocomposites: Pathways and mechanisms. *Separation and Purification Technology* **2014,** *135*, 35-41.

122. Cheng, J.; Vecitis, C. D.; Park, H.; Mader, B. T.; Hoffmann, M. R., Sonochemical degradation of perfluorooctane sulfonate (PFOS) and perfluorooctanoate (PFOA) in landfill groundwater: environmental matrix effects. *Environmental science & technology* **2008,** *42*, 8057-8063.

123. Yang, B.; Jiang, C.; Yu, G.; Zhuo, Q.; Deng, S.; Wu, J.; Zhang, H., Highly efficient electrochemical degradation of perfluorooctanoic acid (PFOA) by F-doped Ti/SnO2 electrode. *Journal of hazardous materials* **2015,** *299*, 417-424.

124. Nabi, I.; Fu, Z.; Li, K.; Cheng, H.; Zhang, L., A comparative study of bismuth-based photocatalysts with titanium dioxide for perfluorooctanoic acid degradation. *Chinese Chemical Letters* **2019**.

125. Lin, J.-C.; Hu, C.-Y.; Lo, S.-L., Effect of surfactants on the degradation of perfluorooctanoic acid (PFOA) by ultrasonic (US) treatment. *Ultrasonics sonochemistry* **2016,** *28*, 130-135.

126. Wang, Y.; Zhang, P.; Pan, G.; Chen, H., Ferric ion mediated photochemical decomposition of perfluorooctanoic acid (PFOA) by 254 nm UV light. *Journal of hazardous materials* **2008,** *160*, 181-186.

127. Gomez-Ruiz, B.; Ribao, P.; Diban, N.; Rivero, M. J.; Ortiz, I.; Urtiaga, A., Photocatalytic degradation and mineralization of perfluorooctanoic acid (PFOA) using a composite TiO2− rGO catalyst. *Journal of hazardous materials* **2018,** *344*, 950-957.

128. Ma, Q.; Liu, L.; Cui, W.; Li, R.; Song, T.; Cui, Z., Electrochemical degradation of perfluorooctanoic acid (PFOA) by Yb-doped Ti/SnO 2–Sb/PbO 2 anodes and determination of the optimal conditions. *Rsc Advances* **2015,** *5*, 84856-84864.

129. Liang, X.; Cheng, J.; Yang, C.; Yang, S., Factors influencing aqueous perfluorooctanoic acid (PFOA) photodecomposition by VUV irradiation in the presence of ferric ions. *Chemical Engineering Journal* **2016,** *298*, 291-299.

130. Zhao, B.; Lv, M.; Zhou, L., Photocatalytic degradation of perfluorooctanoic acid with β-Ga2O3 in anoxic aqueous solution. *Journal of Environmental Sciences* **2012,** *24*, 774-780.

131. Yamada, T.; Taylor, P. H.; Buck, R. C.; Kaiser, M. A.; Giraud, R. J., Thermal degradation of fluorotelomer treated articles and related materials. *Chemosphere* **2005,** *61*, 974-984.

132. Peng, Y.-P.; Chen, H.; Huang, C., The synergistic effect of photoelectrochemical (PEC) reactions exemplified by concurrent perfluorooctanoic acid (PFOA) degradation and hydrogen generation over carbon and nitrogen codoped TiO2 nanotube arrays (CN-TNTAs) photoelectrode. *Applied Catalysis B: Environmental* **2017,** *209*, 437-446.

133. Cui, J.; Gao, P.; Deng, Y., Destruction of Per-and Polyfluoroalkyl Substances (PFAS) with Advanced Reduction Processes (ARPs): A Critical Review. *Environmental Science & Technology* **2020**.

134. Bentel, M. J.; Yu, Y.; Xu, L.; Kwon, H.; Li, Z.; Wong, B. M.; Men, Y.; Liu, J., Degradation of Perfluoroalkyl Ether Carboxylic Acids with Hydrated Electrons: Structure–Reactivity Relationships and Environmental Implications. *Environmental Science & Technology* **2020,** *54*, 2489-2499.

135. Mokh, S.; El Khatib, M.; Koubar, M.; Daher, Z.; Al Iskandarani, M., Innovative SPE-LC-MS/MS technique for the assessment of 63 pharmaceuticals and the detection of antibiotic-resistant-bacteria: A case study natural water sources in Lebanon. *Science of the Total Environment* **2017,** *609*, 830-841.

136. Verplaetse, R.; Henion, J., Quantitative determination of opioids in whole blood using fully automated dried blood spot desorption coupled to on‐line SPE‐LC‐MS/MS. *Drug testing and analysis* **2016,** *8*, 30-38.

137. Shoemaker, J., Method 537. Determination of selected perfluorinated alkyl acids in drinking water by solid phase extraction and liquid chromatography/tandem mass spectrometry (LC/MS/MS). **2009**.

138. Saleem, M.; Biondo, O.; Sretenović, G.; Tomei, G.; Magarotto, M.; Pavarin, D.; Marotta, E.; Paradisi, C., Comparative performance assessment of plasma reactors for the treatment of PFOA; reactor design, kinetics, mineralization and energy yield. *Chemical Engineering Journal* **2020,** *382*, 123031.

139. Javed, H.; Lyu, C.; Sun, R.; Zhang, D.; Alvarez, P. J., Discerning the inefficacy of hydroxyl radicals during perfluorooctanoic acid degradation. *Chemosphere* **2020**, 125883.

140. Shi, H.; Wang, Y.; Li, C.; Pierce, R.; Gao, S.; Huang, Q., Degradation of Perfluorooctanesulfonate by Reactive Electrochemical Membrane Composed of Magneli Phase Titanium Suboxide. *Environmental science & technology* **2019,** *53*, 14528-14537.

141. Rivero, M. J.; Ribao, P.; Gomez-Ruiz, B.; Urtiaga, A.; Ortiz, I., Comparative performance of TiO2-rGO photocatalyst in the degradation of dichloroacetic and perfluorooctanoic acids. *Separation and Purification Technology* **2020**, 116637.

142. Li, T.; Wang, C.; Wang, T.; Zhu, L., Highly efficient photocatalytic degradation toward perfluorooctanoic acid by bromine doped BiOI with high exposure of (001) facet. *Applied Catalysis B: Environmental* **2020,** *268*, 118442.

143. Liu, Y.; Fan, X.; Quan, X.; Fan, Y.; Chen, S.; Zhao, X., Enhanced perfluorooctanoic acid degradation by electrochemical activation of sulfate solution on B/N codoped diamond. *Environmental science & technology* **2019,** *53*, 5195-5201.